

A MEASUREMENT OF THE $\tau^- \rightarrow K^- \nu_\tau$ BRANCHING RATIO USING THE
OPAL DETECTOR AT LEP

by

Sherry Meleah Jean Towers

B. Sc., Simon Fraser University, 1991

ACCEPTED

FACULTY OF GRADUATE STUDIES

DEAN

A THESIS SUBMITTED IN PARTIAL FULFILLMENT OF

THE REQUIREMENTS FOR THE DEGREE OF

MASTER OF SCIENCE

IN THE DEPARTMENT OF PHYSICS AND ASTRONOMY

WE ACCEPT THIS THESIS AS CONFORMING

TO THE REQUIRED STANDARD

DR. D. PITMAN, SUPERVISOR (DEPARTMENT OF PHYSICS)

DR. R. KEELER, DEPARTMENTAL MEMBER (DEPARTMENT OF PHYSICS)

DR. T. GOUGH, OUTSIDE MEMBER (DEPARTMENT OF CHEMISTRY)

DR. M. RONEY, ADDITIONAL MEMBER (INSTITUTE OF PARTICLE PHYSICS)

DR. J. PRENTICE, EXTERNAL EXAMINER (UNIVERSITY OF TORONTO)

© SHERRY TOWERS, 1993

UNIVERSITY OF VICTORIA

ALL RIGHTS RESERVED. THESIS MAY NOT BE REPRODUCED IN WHOLE OR IN PART,
BY PHOTOCOPY OR OTHER MEANS, WITHOUT THE PERMISSION OF THE AUTHOR.

QC 793.5
M42T6

Table of Contents

Abstract	v
Acknowledgements	vii
List of Tables	viii
List of Figures	ix
1 Introduction	1
1.1 The Standard Model	2
1.2 The τ Lepton	5
2 The OPAL Detector	11
2.1 The Central Detector	12

2.1.1	Drift Chambers	14
2.1.2	The OPAL Jet Chamber	14
2.2	The Electromagnetic Calorimeter	22
2.3	The Hadronic Calorimeter	24
2.4	The Muon Chambers	25
3	Measurement of the $\tau^- \rightarrow K^- \nu_\tau$ branching ratio	26
3.1	Monte Carlo and the Predicted Mean Energy Loss	27
3.1.1	Parameterisation of the Predicted Mean Energy Loss	27
3.1.2	Monte Carlo	33
3.2	Calculation of the $\tau^- \rightarrow K^- \nu_\tau$ Relative Branching Ratio	39
3.2.1	Evaluation of the systematic errors	45
4	Discussion of the results	50
5	Conclusions	53

Bibliography	55
Appendix A	56
A.1 Selection of $e^+e^- \rightarrow \tau^+\tau^-$ Candidates	57
A.1.1 Selection of $\tau^- \rightarrow \mu^- \bar{\nu}_\mu \nu_\tau$ Candidates	59
A.1.2 Selection of $\tau^- \rightarrow \pi^- (K^-) \nu_\tau$ Candidates	62

Supervisor: Dr. D. Pitman

ABSTRACT

This thesis describes the determination of the $\tau^- \rightarrow K^- \nu_\tau$ and $\tau^- \rightarrow \pi^- \nu_\tau$ branching ratios using data collected by the OPAL detector at the LEP e^+e^- collider during the years 1990 and 1991.

From a sample of 11381 $e^+e^- \rightarrow \tau^+\tau^-$ candidates, a sample of 1242 $\tau^- \rightarrow \pi^-(K^-)\nu_\tau$ candidates was selected (where this notation refers to a tau decay to either a charged pion or kaon final state plus a neutrino). In order to distinguish between the pions and the kaons in this sample to determine the $\tau^- \rightarrow K^- \nu_\tau$ and $\tau^- \rightarrow \pi^- \nu_\tau$ branching ratios, the combination of an ionization energy loss measurement and a momentum measurement was used; as a charged particle traverses a gas, it ionizes the gas and deposits a small amount of energy. The energy deposited is proportional to the speed of the particle and therefore, in conjunction with a momentum measurement, the energy loss measurement can be used to distinguish between charged particles of different masses.

This technique yielded a sample of 26 $\tau^- \rightarrow K^- \nu_\tau$ candidates. After efficiencies and backgrounds were estimated using Monte Carlo and data studies, the $\tau^- \rightarrow K^- \nu_\tau$ branching ratio relative to the $\tau^- \rightarrow \pi^-(K^-)\nu_\tau$ branching ratio was determined to be

$$\frac{\Gamma(\tau \rightarrow K \nu)}{\Gamma(\tau \rightarrow \pi(K) \nu)} = 0.087 \pm 0.017^{+0.016}_{-0.017}$$

which yielded the following absolute branching ratios:

$$Br(\tau \rightarrow K \nu) = 0.0106 \pm 0.0021^{+0.0020}_{-0.0021} \quad \text{and} \quad Br(\tau \rightarrow \pi \nu) = 0.1113 \pm 0.0034 \pm 0.0040$$

which are in good agreement with the previous world averages [5]:

$$Br(\tau \rightarrow K \nu) = 0.0067 \pm 0.0023 \quad \text{and} \quad Br(\tau \rightarrow \pi \nu) = 0.116 \pm 0.004$$

Examiners:

[REDACTED]
Dr. D. Pitman, Supervisor (Department of Physics)

[REDACTED]
Dr. R. Keeler, Departmental Member (Department of Physics)

[REDACTED]
Dr. T. Gough, Outside Member (Department of Chemistry)

[REDACTED]
Dr. M. Roney, Additional Member (Institute of Particle Physics)

[REDACTED]
Dr. J. Prentice, External Examiner (University of Toronto)

Acknowledgements

This thesis would not have been possible without the help of a number of people. I would like to thank my supervisor, Dale Pitman, for being there for me when things went wrong and also for all the weekly long distance chats that were an invaluable aid in preparing this thesis.

I am deeply indebted to Mike Roney for all the help he provided in both the research and preparation of this thesis and the many hours he has spent with me discussing this topic.

I would also like to thank M. Hauschild for the informative discussions regarding the parameterisation of the energy loss.

Finally, I would like to thank my husband, Matthew, for all his love, support, and patience over the past year.

List of Tables

3.1	The two predicted energy loss parameters determined from a maximum likelihood fit to the measured energy loss (in keV/cm) of data samples derived from the $e^+e^- \rightarrow \tau^+\tau^-$ candidate sample.	30
3.2	Parameters used in the calculation of the $\tau^- \rightarrow K^- \nu_\tau$ relative branching ratio. . . .	46
3.3	Monte Carlo generated events used in the calculation of the $\tau^- \rightarrow K^- \nu_\tau$ relative branching ratio.	46
3.4	Data event parameters used in the calculation of the $\tau^- \rightarrow K^- \nu_\tau$ relative branching ratio.	47
3.5	Change in the $\tau^- \rightarrow K^- \nu_\tau$ relative branching ratio as a function of various systematic studies.	48
3.6	A comparison of the relative branching ratios, number of $\tau^- \rightarrow K^- \nu_\tau$ candidate events, efficiencies, and estimated backgrounds corresponding to three different selection values in dE/dx_{norm}^π	49
A.7	Estimated background contaminations found in the selected $\tau^- \rightarrow \mu^- \bar{\nu}_\mu \nu_\tau$ candidate events in the 1990 and 1991 data.	61
A.8	Estimated background contaminations found in the selected $\tau^- \rightarrow \pi^- (K^-) \nu_\tau$ candidate events in the 1990 and 1991 data.	64

List of Figures

1.1	Two like charges interact via the electromagnetic force; an example of interaction through the exchange of a gauge boson (in this case a photon).	3
1.2	An example of the flavour-changing charged weak interaction: The u quark emits a W^+ which subsequently changes the quark flavour to d' . The electron then absorbs the W^+ , thus changing its flavour to an electron neutrino.	6
1.3	(a) Feynman diagram depicting the annihilation of an e^+e^- pair to form a Z^0 or photon, which then decays to a $\tau^+\tau^-$ pair. (b) Feynman diagram depicting the Cabibbo-suppressed charged weak decay of a τ lepton to a neutrino and the quark-antiquark pair which forms a charged kaon.	8
2.4	General layout of the OPAL detector.	13
2.5	Schematic of one of the cells of the OPAL jet chamber. There are 24 such cells in the $r\phi$ plane. Large dots in the anode plane denote the field shaping potential wires, and X's denote the anode wires. The drift distance between the cathode and anode planes ranges from 3 cm at the innermost wires to 25 cm at the outermost wires. The drawing is not to scale.	15
2.6	A schematic of the OPAL jet chamber.	16

2.7	The ratio of the kaon to pion speeds, β_K/β_π , versus momentum. Notice that at high momenta the ratio is almost exactly equal to one whereas at low momenta the two speeds are quite different.	20
2.8	(a) A typical plot of energy loss, dE/dx , versus momentum. (b) dE/dx versus momentum for various particles in the OPAL jet chamber. . . .	21
2.9	The dimensionless quantity, particle separation power D , as a function of momentum for various particles in the OPAL jet chamber. Note that the best separation between pions and kaons occurs below about 20 GeV/c.	23
3.10	(a) dE/dx_{meas} versus dE/dx_{pred} for the data $\tau \rightarrow \mu \bar{\nu} \nu$ candidate sample between 3.5 to 20 GeV/c. Note that the slope, $A1$, is consistent with one and the intercept, $A0$, is consistent with zero, as would be expected if dE/dx_{pred} was predicting the muon energy loss correctly. (b) $(dE/dx_{meas} - dE/dx_{pred})$ versus momentum for the $\tau \rightarrow \mu \bar{\nu} \nu$ candidate sample between 3.5 to 20 GeV/c. Note the slope and intercept of the fitted line are both consistent with zero, again indicating that dE/dx_{pred} is modelling the data well. . .	32
3.11	dE/dx_{norm}^K of the rough kaon sample (normalized to kaon dE/dx using dE/dx_{pred} with the kaon mass and the parameters obtained from the fit). Note that the mean is consistent with zero and the width is close to one as would be expected if dE/dx_{pred} was predicting kaon dE/dx well.	34

3.12	(a) Distribution in $\cos \theta$ for data (solid line) and Monte Carlo (dashed line) generated $\tau \rightarrow \mu \bar{\nu} \nu$ candidate samples.	
	(b) Distribution in ϕ for data (solid line) and Monte Carlo (dashed line) generated $\tau \rightarrow \mu \bar{\nu} \nu$ candidate samples.	
	(c) Momentum distribution for data (solid line) and Monte Carlo (dashed line) generated $\tau \rightarrow \mu \bar{\nu} \nu$ candidate samples.	
	$\tau \rightarrow e \bar{\nu} \nu$ and $\tau \rightarrow \pi(K) \nu$ samples show similar agreement between data and Monte Carlo generated events.	35
3.13	(a) $N_{dE/dx}$ distribution for data $\tau \rightarrow \mu \bar{\nu} \nu$ candidate sample with local ϕ between 0° to 3° (solid line) and 9° to 12° (dashed line). In both cases the momentum is between 20 to 45 GeV/c.	
	(b) $N_{dE/dx}$ distribution for data $\tau \rightarrow \mu \bar{\nu} \nu$ candidate sample with momentum between 20 to 45 GeV/c (solid line) and 2 to 5 GeV/c (dashed line). In both cases local ϕ is between 9° to 12° .	
	For presentation purposes all histograms have been normalised such that the area under each histogram is equal to one.	37
3.14	(a) Normalized dE/dx distribution for the $\tau \rightarrow \mu \bar{\nu} \nu$ candidate sample between 3.5 to 20 GeV/c for both the data (points) and the Monte Carlo generated events (histogram).	
	(b) Normalized dE/dx distribution for the $\tau \rightarrow \pi(K) \nu$ candidate sample between 3.5 to 20 GeV/c for both the data (points) and the Monte Carlo generated events (histogram).	38
3.15	Momentum distribution of the $\tau \rightarrow \pi(K) \nu$ candidate sample for both the data (points) and Monte Carlo generated events (histogram). Dotted lines denote the momentum range in which $\tau \rightarrow K \nu$ candidates were selected out of the $\tau \rightarrow \pi(K) \nu$ sample. . . .	40

3.16	(a) Efficiency for selecting $\tau \rightarrow K\nu$ events out of the $\tau \rightarrow \pi(K)\nu$ candidate sample (<i>after</i> the momentum selection) as a function of the selection value in normalised dE/dx .	
	(b) Estimated background in the $\tau \rightarrow K\nu$ candidate sample as a function of the selection value in normalised dE/dx	42
3.17	Energy loss distribution of the $\tau \rightarrow \pi(K)\nu$ candidate sample normalized to a pion hypothesis for both the data (points) and Monte Carlo generated events (histogram). The shaded portion of the histogram represents the non $\tau \rightarrow K\nu$ events in the Monte Carlo generated $\tau \rightarrow \pi(K)\nu$ candidate sample. All events below the normalized energy loss selection value denoted by the arrow were selected as $\tau \rightarrow K\nu$ candidates.	43
3.18	Energy loss distribution of the $\tau \rightarrow K\nu$ candidate sample normalized to a pion hypothesis for both the data (points) and Monte Carlo generated events (histogram). The shaded portion of the histogram represents the non $\tau \rightarrow K\nu$ events in the Monte Carlo generated $\tau \rightarrow K\nu$ candidate sample.	44

Chapter 1

Introduction

The Standard Model of particle physics describes the interaction of particles under the influence of the strong, electromagnetic, and weak forces. The strong interaction is described by the theory of Quantum Chromodynamics (QCD), and the electromagnetic and weak interactions are described by a single, unified *electroweak* theory.

This thesis examines some electroweak aspects of the Standard Model through the study of the weak decay of the τ lepton to a single kaon plus a neutrino final state, using data collected by the OPAL experiment at the LEP e^+e^- collider during the years 1990 and 1991.

The following sections will give a brief introduction to the Standard Model, the tau lepton, and a short outline of the analysis presented in this thesis. Chapter two is a description of the OPAL detector and how it is used to distinguish between particle species, and chapter three describes the analysis in detail.

1.1 The Standard Model

Excellent reviews of the Standard Model can be found in many texts (for instance [1] and [2]), therefore only a short overview will be given here.

The basic particles in nature are the fundamental fermions and gauge bosons. The fundamental fermions (spin 1/2, pointlike, structureless particles) can be classed into *quarks* and *leptons* and they interact with each other through the exchange of gauge bosons. This is shown graphically in figure 1.1 which is an example of a *Feynman diagram*. Feynman diagrams are an important theoretical tool used to calculate the probability of occurrence of various interactions. In this thesis the time axis in Feynman diagrams will always point towards the right. A particle depicted as moving *backwards* in time in a Feynman diagram can also be considered as an *antiparticle* moving *forwards* in time.

Both quarks and leptons are solutions to the Dirac equation (a formula describing free spin 1/2 particles), and both have antimatter analogues. Quarks carry colour charge which enables them to interact via the strong force through the exchange of a gauge boson called a *gluon*. An aspect of the strong interaction is that free quarks are never directly observed in the laboratory. Rather they are always bound together into composite objects called *hadrons*. From current observations, a hadron is either a bound state of a quark and an antiquark pair, called a *meson*, or a three-quark bound state called a *baryon*. Leptons are ‘colourless’ and hence do not interact via the strong force. There are six currently known kinds or *flavours* of quarks and leptons and they fall into three families or *doublets*¹:

$$\begin{pmatrix} u \\ d \end{pmatrix} \quad \begin{pmatrix} c \\ s \end{pmatrix} \quad \begin{pmatrix} t \\ b \end{pmatrix}$$

$$\begin{pmatrix} \nu_e \\ e \end{pmatrix} \quad \begin{pmatrix} \nu_\mu \\ \mu \end{pmatrix} \quad \begin{pmatrix} \nu_\tau \\ \tau \end{pmatrix}$$

¹Antiparticle conjugates to quarks and neutrinos are denoted with a bar notation. For example, the antiparticle conjugate to the d quark is the \bar{d} quark

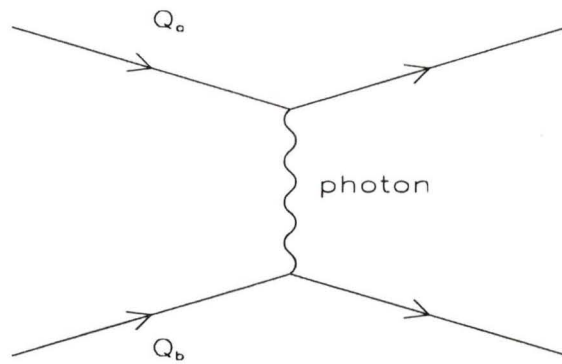


Figure 1.1: Two like charges interact via the electromagnetic force; an example of interaction through the exchange of a gauge boson (in this case a photon).

where the second and third set of doublets are simply higher mass replicas of the first. The upper quarks in each quark doublet have electric charge $q = 2/3e$ and the lower quarks have electric charge $q = -1/3e$ (e is the magnitude of the electron's charge). The upper leptons in each lepton doublet are electrically neutral and are referred to as *neutrinos*. Neutrino masses have been found to be consistent with zero within experimental limits. The lower leptons in each lepton doublet have electric charge $q = -e$. The quarks and the charged leptons can interact via the electromagnetic force through the exchange of a gauge boson called a *photon*.

Both leptons and quarks can interact via the weak force. The weak interaction can be classified into the *neutral* weak force and the *charged* weak force. The Z^0 and the W^\pm are the gauge bosons associated with the neutral and charged weak interactions, respectively.

The quark states which participate in the weak interaction are not the same as the quark states which are seen bound into hadrons in the laboratory. The former are called the quark *weak eigenstates* and the latter are called the quark *mass eigenstates*. The quark weak eigenstates (denoted with prime notation as d' , s' , and b') are related to the mass eigenstates by the transformation:

$$\begin{pmatrix} d' \\ s' \\ b' \end{pmatrix} = V * \begin{pmatrix} d \\ s \\ b \end{pmatrix} \quad (1.1)$$

where V is a 3×3 matrix known as the *Cabibbo-Kobayashi-Maskawa mixing matrix*. By convention only the quarks with mass $q = -1/3e$ have distinct weak and mass eigenstates.

It has been found experimentally that only *left-handed* quarks and leptons (or their *right-handed* antiparticle conjugates) can couple to the W^\pm boson and therefore participate in the charged weak interaction. In the electroweak Standard Model the left-handed quarks and leptons are classed into doublets:

$$\begin{pmatrix} u \\ d' \end{pmatrix}_L \quad \begin{pmatrix} c \\ s' \end{pmatrix}_L \quad \begin{pmatrix} t \\ b' \end{pmatrix}_L$$

$$\begin{pmatrix} \nu_e \\ e \end{pmatrix}_L, \begin{pmatrix} \nu_\mu \\ \mu \end{pmatrix}_L, \begin{pmatrix} \nu_\tau \\ \tau \end{pmatrix}_L$$

The W^\pm boson can only couple to quarks or leptons within a left-handed doublet. One can think of the charged weak interaction as changing the flavour of a quark or lepton; as a left-handed quark or lepton in a doublet emits or absorbs a W^\pm boson, the flavour of the particle changes to the second flavour within its doublet. Thus, emitting or absorbing a W^\pm changes an electron into an electron neutrino, a u quark into a d' quark and so on. Figure 1.2 shows an example of the flavour-changing charged weak interaction.

The right-handed quarks and charged leptons (there are no right-handed neutrinos) are singlets:

$$(e_R), (\mu_R), (\tau_R), (u_R), (d_R), (c_R), (s_R), (t_R), (b_R).$$

The neutral weak interaction can couple to either right- or left-handed quarks and leptons and the emission or absorption of a Z^0 boson *does not* change the flavour of a particle.

1.2 The τ Lepton

Since its discovery in 1975 by M. Perl et al. at SPEAR with the MARK I detector [3] [4], the τ lepton has provided important opportunities for testing fundamental aspects of weak interactions. In particular, the study of the weak decays of the τ lepton to hadronic final states allows us to examine the couplings of the W^\pm boson to quarks.

The τ mass is such that it is heavy enough to allow charged weak decays to hadronic final states, but only heavy enough to allow decay into the quarks in the lightest left-handed doublet, the u and the d' quarks (the mass of the lightest hadron, the pion, is about $0.14 \text{ GeV}/c^2$; for comparison, the mass of the μ lepton is about $0.11 \text{ GeV}/c^2$, and the mass of

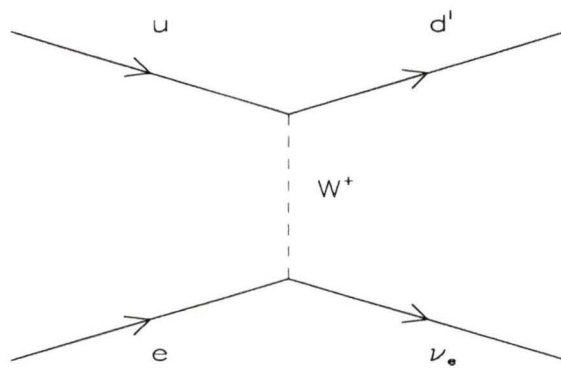


Figure 1.2: An example of the flavour-changing charged weak interaction: The u quark emits a W^+ which subsequently changes the quark flavour to d' . The electron then absorbs the W^+ , thus changing its flavour to an electron neutrino.

the τ lepton is about $1.8 \text{ GeV}/c^2$). The weak eigenstate d' quark is a linear combination of quark mass eigenstates and, to a good approximation, can be expressed as:

$$d' = d \cdot \cos \theta_C + s \cdot \sin \theta_C$$

where θ_C is a parameter called the *Cabibbo angle* (the b quark portion of d' is neglected since its coefficient is very small). Experimentally θ_C is known to be about 13° [5]. Thus one obtains

$$d' = 0.97d + 0.22s.$$

Thus *most* of the time the τ lepton will decay via the charged weak interaction to a combination of u and d quark mass eigenstates. This is known as a *Cabibbo-enhanced decay mode*. Sometimes, however, the τ lepton will decay weakly to a combination of u and s quark mass eigenstates. This case is known as a *Cabibbo-suppressed decay mode*.

This thesis will examine Cabibbo-suppressed τ decay by determining the branching ratio of the decay of the τ lepton to a neutrino and a charged kaon. This decay will often be referred to in this thesis in the notation $\tau^- \rightarrow K^- \nu_\tau$, where this notation also implies the charged conjugate decay $\tau^+ \rightarrow K^+ \bar{\nu}_\tau$ (sometimes the shorthand notation $\tau \rightarrow K \nu$ will also be used). The Feynman diagram depicting the $\tau^- \rightarrow K^- \nu_\tau$ decay is shown in figure 1.3 (b). A branching ratio is the probability that a particle will decay to a particular set of final states.

Previous measurements of the τ Cabibbo-suppressed decay to the charged K meson plus a neutrino have been performed by both the DELCO [6] and the MARKII [7] experiments. Both measurements, however, were based upon low statistics (15 and 16 signal events, respectively). In order to study this decay mode of the τ particle better, an ample production of τ leptons in a low background environment is needed.

Such an environment can be found at the LEP collider at CERN; large numbers of τ pairs are produced through e^+e^- annihilation at the Z^0 resonance (as shown in figure 1.3 (a)). Features of the OPAL detector at LEP enable the identification of these τ pairs with high efficiency and low background [14].

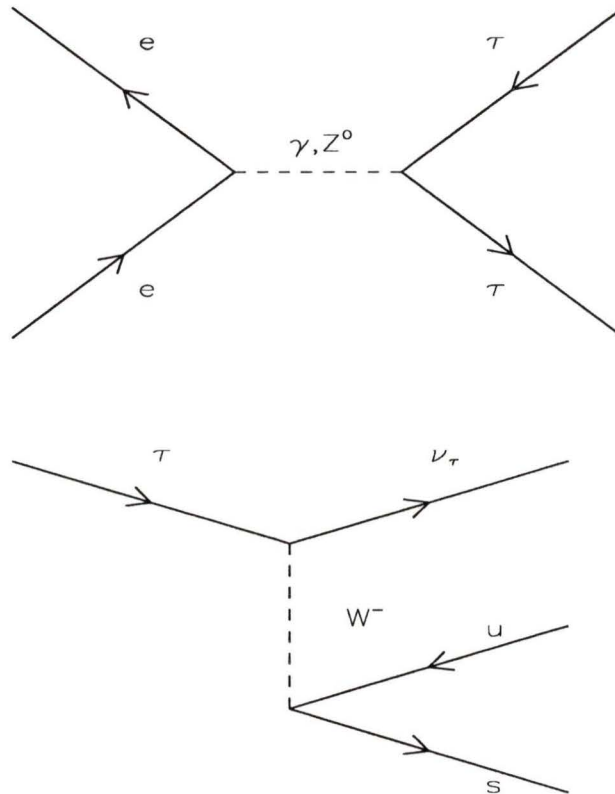


Figure 1.3: (a) Feynman diagram depicting the annihilation of an e^+e^- pair to form a Z^0 or photon, which then decays to a $\tau^+\tau^-$ pair.

(b) Feynman diagram depicting the Cabibbo-suppressed charged weak decay of a τ lepton to a neutrino and the quark-antiquark pair which forms a charged kaon.

In this thesis a measurement of the $\tau^- \rightarrow K^- \nu_\tau$ branching ratio relative to the sum of the $\tau^- \rightarrow \pi^- \nu_\tau$ and $\tau^- \rightarrow K^- \nu_\tau$ branching ratios (this sum is also known as the $\tau^- \rightarrow \pi^- (K^-) \nu_\tau$ branching ratio) will be presented using data from approximately 23000 τ lepton decays by the OPAL detector at LEP during the years 1990 and 1991. After this *relative branching ratio* has been extracted, an absolute branching ratio for $\tau^- \rightarrow K^- \nu_\tau$ will then be calculated.

From the τ candidate sample, a sample of $\tau^- \rightarrow \pi^- (K^-) \nu_\tau$ candidates is selected. To perform the branching ratio measurement, we separate the pions and kaons in that sample by exploiting the fact that charged particles traversing a gas ionize the gas and lose a small amount of energy; the amount of energy lost is proportional to the speed of the particle and, in conjunction with a momentum measurement, can be used to distinguish between particles of different masses.

The general form of the relative branching ratio is given by [8]

$$\frac{\Gamma(\tau^- \rightarrow K^- \nu_\tau)}{\Gamma(\tau^- \rightarrow \pi^- (K^-) \nu_\tau)} = \frac{f_K^2 \sin^2 \theta_C f_{\tau \rightarrow K \nu}^{kin}}{f_K^2 \sin^2 \theta_C f_{\tau \rightarrow K \nu}^{kin} + f_\pi^2 \cos^2 \theta_C f_{\tau \rightarrow \pi \nu}^{kin}}$$

where

$$f_{\tau \rightarrow (K, \pi) \nu}^{kin} = \frac{m_\tau^3}{2} \left[1 - \frac{m_{(K, \pi)}^2}{m_\tau^2} \right]^2 \quad (1.2)$$

and f_K and f_π are factors (often referred to as *form factors*) which take into account the fact that the quark decay products are not free (as lepton decay products would be) but rather are bound into a hadronic final state. Neither f_K , f_π , nor θ_C can be derived from theory and therefore the phenomenology of hadronic τ decays depends on these quantities being well measured by some other decay processes or interactions.

Two such interactions which can be used are the $\pi^- \rightarrow \mu^- \bar{\nu}_\mu$ and $K^- \rightarrow \mu^- \bar{\nu}_\mu$ decays. The ratios of the branching ratios of these decays is equal to

$$\frac{Br(K \rightarrow \mu \nu)}{Br(\pi \rightarrow \mu \nu)} = \tan^2 \theta_C \frac{f_K^2 m_\pi^3 \tau_K}{f_\pi^2 m_K^3 \tau_\pi} \frac{[m_K^2 - m_\mu^2]^2}{[m_\pi^2 - m_\mu^2]^2} \quad (1.3)$$

where τ_π and τ_K are the lifetimes of the charged pion and kaon, respectively. When combined with 1.2 this yields the prediction

$$\frac{\Gamma(\tau \rightarrow K\nu)}{\Gamma(\tau \rightarrow \pi\nu)} = \frac{m_K^3 \tau_\pi (m_\tau^2 - m_K^2)^2 (m_\pi^2 - m_\mu^2)^2 Br(K \rightarrow \mu\nu)}{m_\pi^3 \tau_K (m_\tau^2 - m_\pi^2)^2 (m_K^2 - m_\mu^2)^2 Br(\pi \rightarrow \mu\nu)} = 0.0653 \pm 0.0007.$$

Chapter 2

The OPAL Detector

OPAL (Omni Purpose Apparatus at LEP) is one of four large detectors built for the e^+e^- storage ring LEP at CERN. Its purpose is to detect all interactions occurring in e^+e^- collisions at a centre-of-mass energy of about 90 GeV and to achieve efficient and accurate reconstruction and classification of events. A full description of the OPAL detector can be found in reference [9].

Some main features of the detector include:

- A central tracking system to measure charged particle momentum, track direction, and energy loss. The momentum and energy loss measurements are used in this thesis to distinguish between pions and kaons in the $\tau^- \rightarrow \pi^- (K^-) \nu_\tau$ event sample.
- A time-of-flight (TOF) system which is used in this thesis to reject cosmic ray backgrounds in the event samples.
- An electromagnetic calorimeter (ECAL) constructed of lead glass blocks. The ECAL is primarily used in this thesis to aid in electron and photon identification and subsequent rejection of events from the $\tau^- \rightarrow \pi^- (K^-) \nu_\tau$ candidate sample which include either an electron or π^0 .
- A hadron sampling calorimeter (HCAL) constructed of layers of iron absorber, with gaps between the plates which are instrumented with streamer tubes. The HCAL is used in this thesis to distinguish between hadrons and muons.

- A muon detector which is used in this thesis to identify muons.

Further discussion of each of these features can be found in the sections below.

The general layout of the OPAL detector is shown in figure 2.4 indicating the location and relative size of various components. Also shown in figure 2.4 is the OPAL coordinate system; the x axis is horizontal and points to the centre of LEP, the z axis lies along the e^- beam direction, and the y axis is approximately vertical (since the LEP ring is inclined at an angle of 13.9 mrad relative to the horizontal plane). The polar angle, θ , is measured from the z axis, and the azimuthal angle, ϕ , is measured from the x axis in the xy plane.

2.1 The Central Detector

The central tracking system of the OPAL detector is designed to accurately measure the direction, momentum, and energy loss, dE/dx , of charged particles. This is achieved using drift chamber technology. In order to facilitate the discussion of the central detector, the short description of a typical drift chamber found in the section below might be helpful. It is the momentum and energy loss measurements which are essential to distinguish between pions and kaons in this analysis and therefore determine the $\tau^- \rightarrow K^- \nu_\tau$ branching ratio.

The central detector consists of three parts: a vertex chamber close to the beam pipe designed to give accurate reconstructions of primary and secondary event vertices; a large drift chamber, also known as the *jet chamber*, which is used to accurately determine the direction and energy loss of charged particles; and the z chamber which is used to accurately determine the z coordinate of charged particles leaving the central detector. The central detector is surrounded by a solenoidal coil which produces an axial field of 0.435 T. Further discussions of the components of the central detector which are used in this analysis can be found in the sections after the general drift chamber discussion.

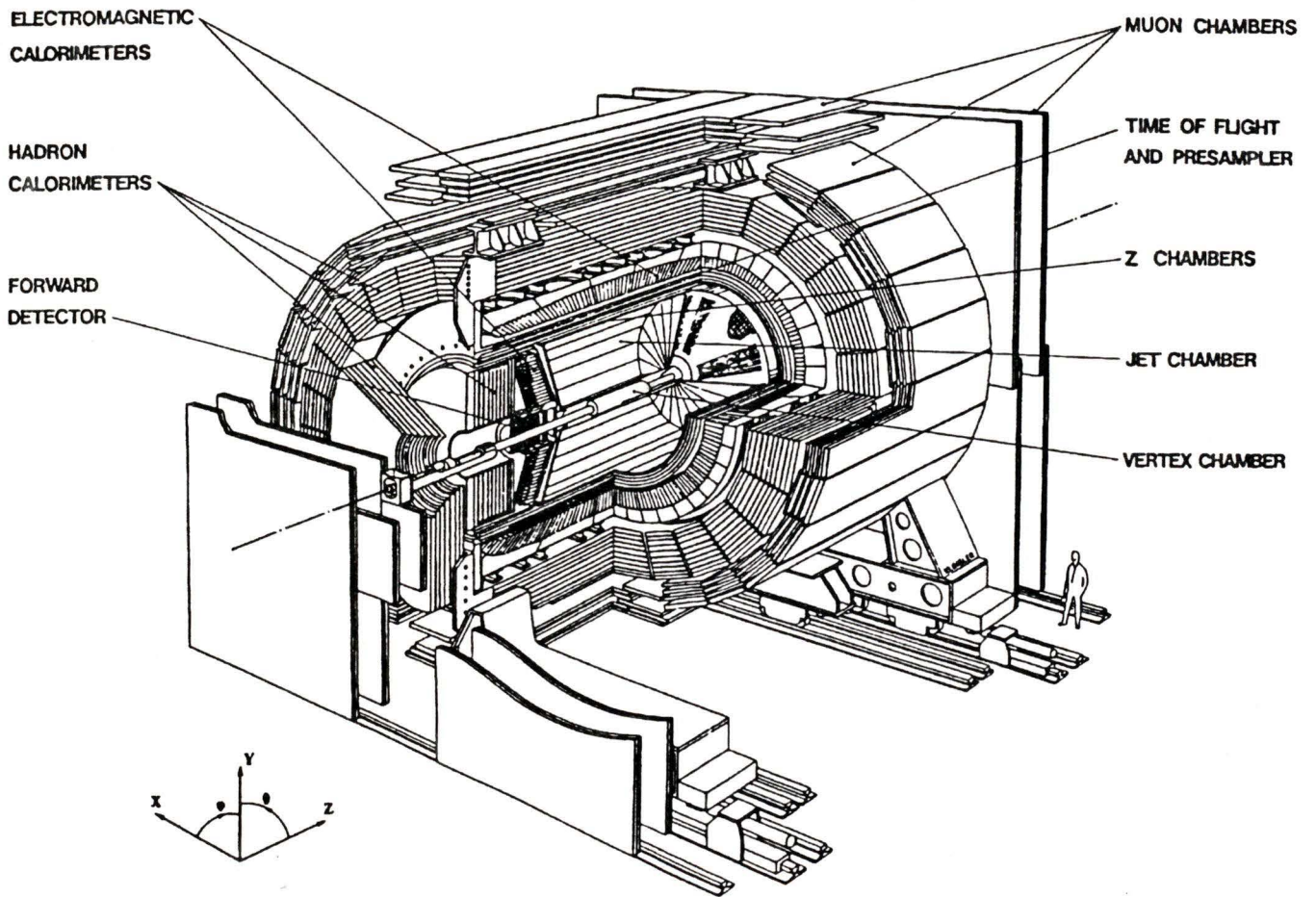


Figure 2.4: General layout of the OPAL detector.

2.1.1 Drift Chambers

A schematic of a cell in the OPAL jet chamber is shown in figure 2.5. The drift chamber is filled with a gas (the OPAL jet chamber uses a mixture of 88% argon, 10% methane, and 2% isobutane at 4 bar (the criteria for choosing the gas pressure will be discussed in the next section)) and the wires of the chamber are arranged in such a way to yield a constant electric field of typically less than 1 kV/cm over most of the chamber. As a charged particle traverses the gas inside a drift chamber it ionizes the gas and the electrons from this primary ionization begin to drift towards the high field amplification region near the anode. Typical drift distances are around 10 cm and the drift times are on the order of one or two μs . As the electrons approach the high field region near the anode, they accelerate and begin to cause secondary ionization of the gas. These secondary electrons can then cause tertiary ionization, and so on. This is known as the *avalanche effect*. The *gas gain* is the total number of electrons reaching the anode per initial ion pair. The gas gain of the OPAL jet chamber is approximately 10^4 .

The electron column caused by the passage of the charged particle initially accelerates in the electric field but very quickly reaches a constant velocity known as the *drift velocity*. Thus the collection time of the avalanche gives a measure of the position of the trajectory of the charged particle to an accuracy of typically 0.1 mm. Further, the number of ion pairs created by the particle as it traverses the chamber is directly proportional to the energy lost by the particle in the ionization process. Thus the integrated charge collected at the anode is a measure of the energy loss of the particle.

2.1.2 The OPAL Jet Chamber

The largest component of the OPAL central detector is the jet chamber, a full description of which can be found in references [10] and [11]. The sensitive volume of the chamber is

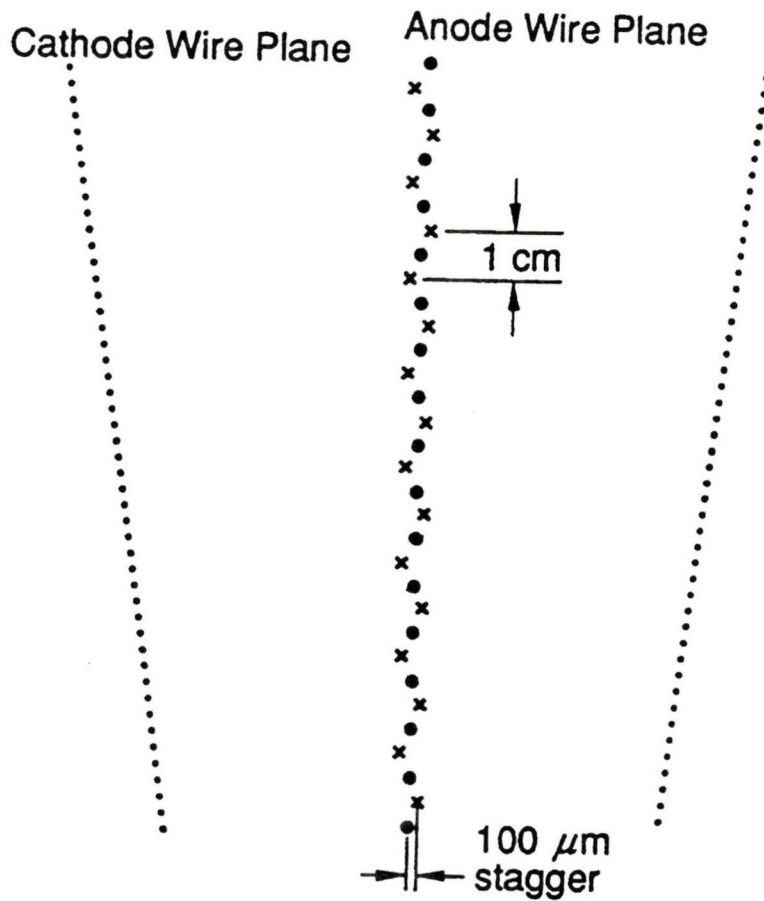


Figure 2.5: Schematic of one of the cells of the OPAL jet chamber. There are 24 such cells in the $r\phi$ plane. Large dots in the anode plane denote the field shaping potential wires, and X's denote the anode wires. The drift distance between the cathode and anode planes ranges from 3 cm at the innermost wires to 25 cm at the outermost wires. The drawing is not to scale.

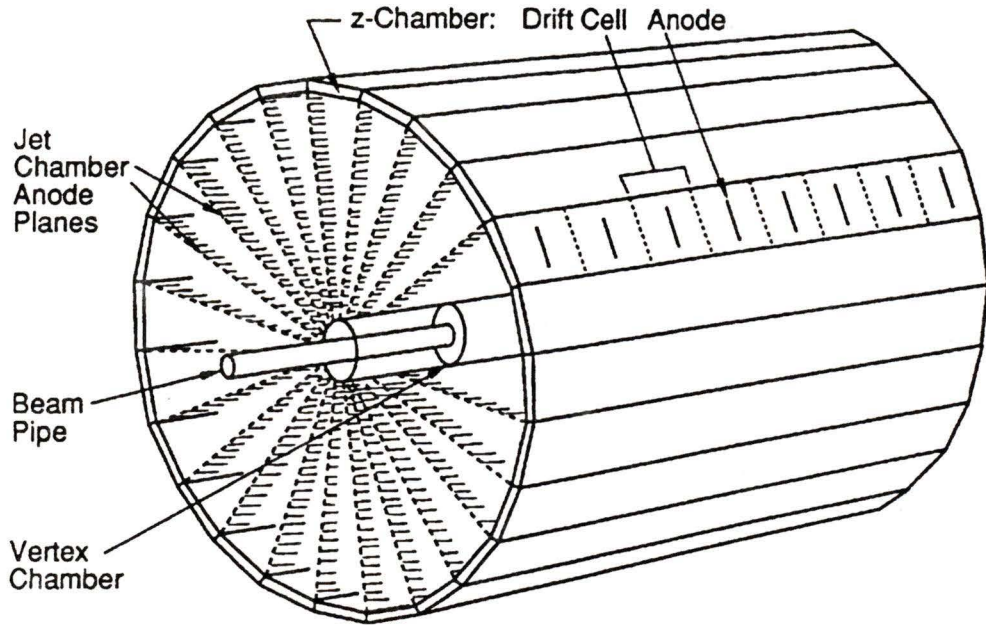


Figure 2.6: A schematic of the OPAL jet chamber.

a cylinder of length approximately 4 m surrounding both the beam pipe and the vertex chamber. The outer diameter is 3.7 m and the inner is 0.5 m.

The chamber is divided into 24 identical sectors in ϕ , each containing 159 anode wires in a radial plane. *Local ϕ* is defined as the ϕ coordinate within a jet chamber cell. Cathode wire planes form the boundaries between adjacent sectors. All wires lie parallel to the beam direction. Schematics of the jet chamber are shown in figures 2.5 and 2.6. The field shaping wires are held at a constant voltage and the cathode wire potentials are graded to produce a constant electric field over most of the chamber. The anode wires are slightly staggered along the anode plane to resolve left/right ambiguities of track trajectories.

The jet chamber is designed to accurately measure the direction and energy loss, dE/dx , of charged particles through multiple sampling of the ionisation along a track. As seen above in the drift chamber discussion, the energy loss of the particle is proportional to the charge deposited on the wire, and the distance of the track from the wire is proportional to the time of arrival of the avalanche at the anode. The momentum of the particle is obtained by measuring the curvature of the particle track in the magnetic field. The spatial resolution of the jet chamber is $\sigma_{x,y} = 135 \mu\text{m}$ [11] which leads to a momentum resolution of

$$\frac{\sigma_p}{p} = \sqrt{0.0004 + (0.0015 * p)^2}$$

where the constant term inside the square root is due to multiple scattering of the charged particle as it traverses the gas. The z coordinate resolution is $\sigma_z = 6 \text{ cm}$ and is obtained by measuring the charge difference at either end of each hit wire. If information from the z chambers is included, the z coordinate resolution is improved to $\sigma_z = 100 - 350 \mu\text{m}$.

A particle traversing the OPAL jet chamber will yield N independent energy loss measurements (where N can be as high as 159) which will be distributed approximately like a Landau distribution. In order to extract the mean energy loss measurement for the particle, we could compare our distribution of N measurements to a Landau distribution using the maximum likelihood method. This procedure is accurate but unfortunately would be prohibitively time consuming to implement as it must be done for each track of every event.

An alternative procedure, which is almost as accurate but is much less time consuming, is to use the method of truncated mean [11]. This method rejects certain percentages of the lowest and highest dE/dx measurements from the N measurements. The mean of the distribution is then calculated from the remaining measurements. The fraction of measurements to be rejected is determined by optimising the dE/dx resolution. For the OPAL jet chamber, the optimum resolution was achieved by truncating the highest 30% of the dE/dx measurements, with no truncation in the low dE/dx portion of the distribution [11].

The resolution of the mean dE/dx measurement using this method depends on the number of energy loss measurements, $N_{dE/dx}$, used in the truncated mean calculation of

dE/dx . It was found for tracks in the OPAL jet chamber that [11]

$$\frac{\sigma(dE/dx)}{(dE/dx)} = A * (N_{dE/dx})^{-0.43} \quad (2.4)$$

where A is a constant. Furthermore, for muons with a momentum of 46 GeV/c it was found that

$$\frac{\sigma(dE/dx)}{(dE/dx)} \sim 3.1\% \quad (2.5)$$

when $N_{dE/dx} \geq 130$.

Ionization Energy Loss and Particle Identification with the OPAL Jet Chamber

The mean energy loss due to ionization is approximately parameterized by the Bethe-Bloch equation [12]

$$dE/dx = -\frac{A_1}{\beta^2} (A_2 + \ln(\gamma^2 \beta^2) - \beta^2 - \delta/2) \quad (2.6)$$

where

$$A_1 = 4\pi N_A r_e^2 m_e c^2 z^2 \frac{Z}{A}$$

and

$$A_2 = \ln\left(\frac{2m_e c^2}{I}\right) \quad (2.7)$$

ze is the charge of the particle passing through a gas with atomic number Z and atomic weight A , m_e and r_e are the mass and classical radius of the electron respectively, and I is known as the *ionization constant* and is approximately equal to $16Z^{0.9}$ eV for $Z > 1$. The quantity δ describes the *density effect* and it depends upon the chemical composition and density of the gas used in the jet chamber. As the energy of a particle increases, δ approaches $\log(\gamma^2)$ plus a constant.

Notice that equation 2.6 depends upon the speed of the particle, β , and not upon the mass. The momentum, however, depends upon both the speed of the particle *and* the mass, therefore the combination of an energy loss and a momentum measurement can be used

to distinguish between charged particles of different masses. This technique is most useful only at momenta below approximately 20 GeV/c, however. To see why, we first look at the functional form of the momentum, p :

$$p = \frac{m\beta}{\sqrt{(1 - \beta^2)}} \quad (2.8)$$

If we have two particle species, A and B , with different masses, m_A and m_B , but the same momentum, we get

$$p = p_A = p_B = \frac{m_A\beta_A}{\sqrt{(1 - \beta_A^2)}} = \frac{m_B\beta_B}{\sqrt{(1 - \beta_B^2)}}$$

which yields the ratio

$$\frac{\beta_A}{\beta_B} = \left(\frac{m_B^2 + p^2}{m_A^2 + p^2} \right)^{1/2} \quad (2.9)$$

A plot of this ratio versus momentum for kaons ($m = 0.4936 \text{ GeV}/c^2$) and pions ($m = 0.1396 \text{ GeV}/c^2$) is shown in figure 2.7. Note that at high momenta the two speeds are nearly equal. Since we saw that dE/dx in equation 2.6 depends upon the speed, the pions and kaons will have virtually the same dE/dx at high momenta. Thus at high momenta the combination of an energy loss and momentum measurement is not useful for discriminating between particles.

At low momenta, however, figure 2.7 shows that the two speeds are quite different. Thus we would expect to be able to efficiently discriminate between pions and kaons for momenta below approximately 20 GeV/c.

A typical plot of the energy loss as a function of momentum is shown in figure 2.8(a). For low momenta, the energy loss shows a characteristic decrease proportional to $1/\beta^2$. Around $\gamma = 3.2$ dE/dx reaches a minimum almost virtually independent of the medium, and then continues with a logarithmic rise (also known as the *relativistic rise region*). At high momenta the energy loss saturates at what is known as the *Fermi plateau*. It is the density effect in equation 2.6 which limits the rise in the energy loss at high momenta to the Fermi plateau. Figure 2.8(b) shows a typical set of plots of the energy loss versus momentum for various particles in the OPAL jet chamber. Notice that, as mentioned above, the energy

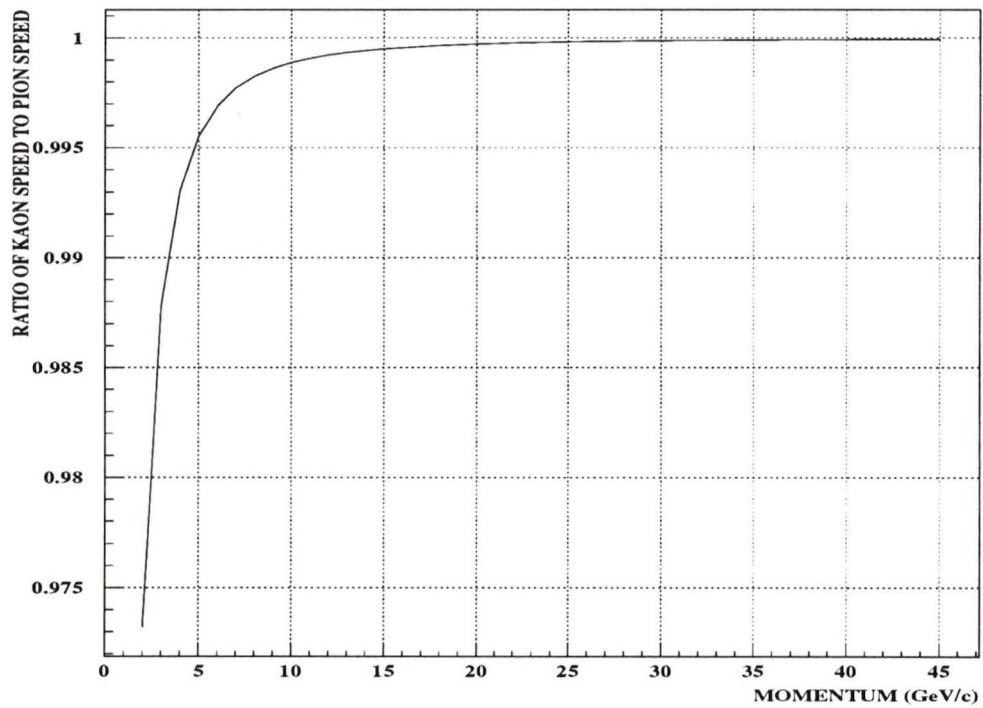


Figure 2.7: The ratio of the kaon to pion speeds, β_K/β_π , versus momentum. Notice that at high momenta the ratio is almost exactly equal to one whereas at low momenta the two speeds are quite different.

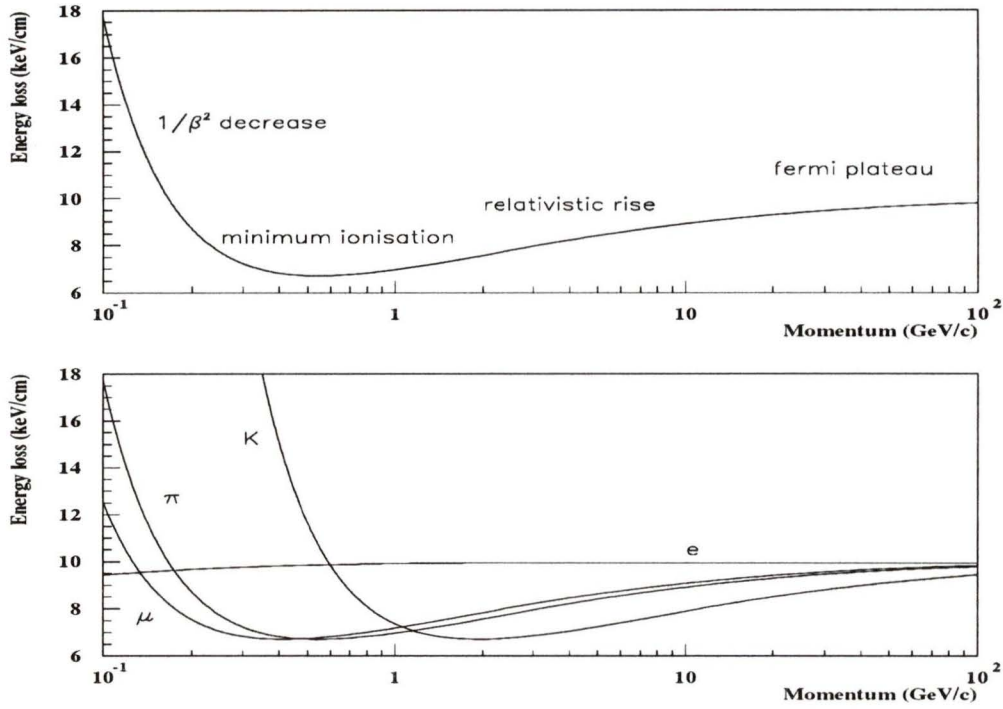


Figure 2.8: (a) A typical plot of energy loss, dE/dx , versus momentum.

(b) dE/dx versus momentum for various particles in the OPAL jet chamber.

loss of the various particle species is nearly the same at high momenta thus making it impossible to distinguish between the particle species using a combination of an energy loss and a momentum measurement.

A measure of how well one can expect to distinguish between two particle species, A and B , using dE/dx is known as the energy loss particle *separation power*, D . The separation power is a dimensionless quantity, defined as

$$D \equiv \frac{(dE/dx)_A - (dE/dx)_B}{\sigma(dE/dx)_B} \quad (2.10)$$

Figure 2.9 shows the particle separation power as a function of momentum for various types of particles in the OPAL jet chamber. Notice that, as mentioned above, the best separation between pions and kaons occurs at momenta less than about 20 GeV/c.

The gas pressure in the OPAL jet chamber has been optimised to provide the best particle separation power. In general, raising the gas pressure improves the dE/dx resolution but reduces the height of the Fermi plateau (which reduces the slope of the relativistic rise). This reduced plateau height has the effect of reducing the difference in energy loss between charged particles of different masses. The optimal pressure for the OPAL jet chamber was found to be 4 bar [11].

A quantity often used in this analysis is normalized dE/dx , defined as follows:

$$dE/dx_{norm} = \frac{dE/dx_{meas} - dE/dx_{pred}}{\sigma(dE/dx)} \quad (2.11)$$

where dE/dx_{meas} is the measured dE/dx , dE/dx_{pred} is the predicted dE/dx for a particular momentum and particle species, and $\sigma(dE/dx)$ is the uncertainty on dE/dx_{meas} . If dE/dx has been normalised assuming a pion, kaon, or muon hypothesis in the calculation of dE/dx_{pred} , then dE/dx_{norm} will be written as dE/dx_{norm}^{π} , dE/dx_{norm}^K , or dE/dx_{norm}^{μ} , respectively.

2.2 The Electromagnetic Calorimeter

The electromagnetic calorimeter at OPAL (ECAL) is constructed of lead glass blocks designed to detect and measure the energies and positions of electrons, positrons, and photons. The glass block assembly is mounted between the solenoid coil and the magnet return yoke. There are also two lead glass assemblies mounted on the endcap resulting in a total ECAL coverage of 98% of 4π . Cherenkov light from the passage of relativistic charged particles through the lead glass is detected by phototubes at the base of each block.

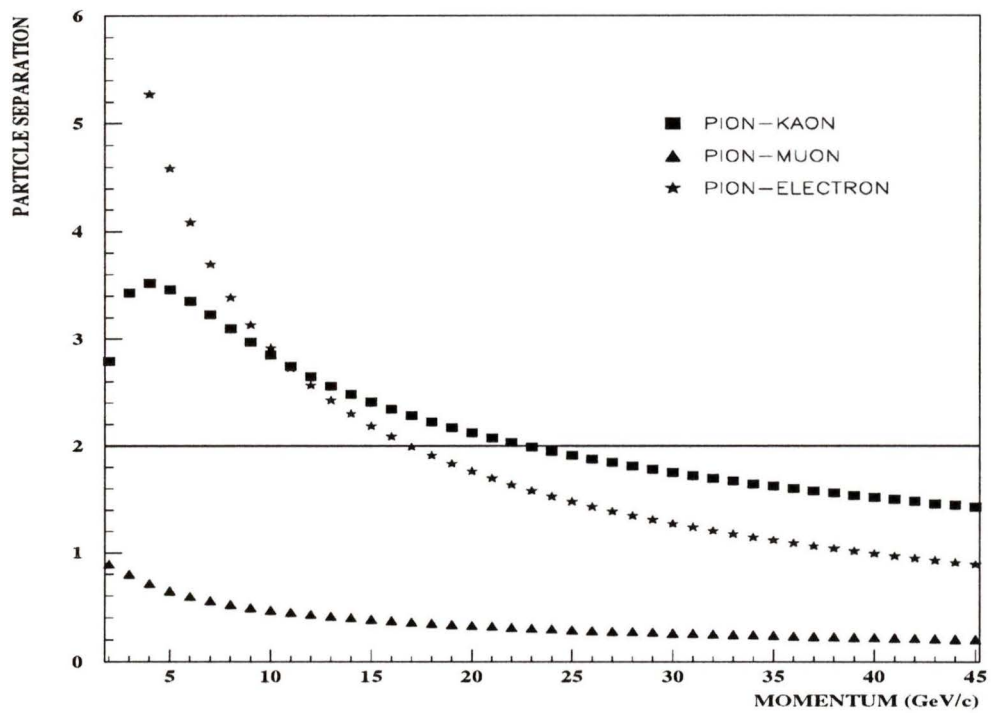


Figure 2.9: The dimensionless quantity, particle separation power D , as a function of momentum for various particles in the OPAL jet chamber. Note that the best separation between pions and kaons occurs below about 20 GeV/c.

The barrel portion of the ECAL covers $|\cos\theta|$ less than 0.82 and the endcap portion covers $|\cos\theta|$ between 0.81 to 0.98.

The presence of ≈ 2 radiation lengths of material in front of the calorimeter (mostly due to the solenoid and central detector pressure vessel) results in most electromagnetic showers initiating before reaching the lead glass. The resulting degradation of the energy and spatial resolution can be corrected for by the use of presampler devices located before the ECAL which are designed to precisely measure the position and energy of showers.

The presampler devices are used in this thesis to reject events in the $\tau^- \rightarrow \pi^- (K^-) \nu_\tau$ candidate sample which are accompanied by a π^0 ; a π^0 decays promptly into two photons which begin to shower in the solenoid coil and hence show a large signal in the presamplers. A charged pion, however, does not typically begin a hadronic shower before reaching the ECAL and hence the presampler signal for a charged pion is much smaller than that of a neutral pion [12].

2.3 The Hadronic Calorimeter

The return yoke of the solenoid is made of welded iron plates, 10 cm thick, with gaps between the plates which are instrumented with streamer tubes and form the barrel hadron calorimeter (HCAL). The final thickness of the HCAL is 1 m which provides 4 or more interaction lengths of absorber over a solid angle of 97% of 4π .

The HCAL consists of three parts, the barrel ($|\cos\theta|$ less than 0.81), the end cap ($|\cos\theta|$ between 0.81 to 0.91), and the pole tip ($|\cos\theta|$ between 0.91 to 0.99) which is constructed of thin, high gain multiwire chambers.

Since hadronic showers usually begin in the ECAL, the hadronic energy is measured

by combining the signals of the ECAL and HCAL. The energy resolution of the HCAL is $120\%/\sqrt{E}$.

2.4 The Muon Chambers

The outside of the HCAL is surrounded by several layers of chambers designed to identify muons by measuring the position and direction of all charged particles leaving the iron absorber of the HCAL. Over the full solid angle, 93% is covered by at least one layer of the muon detector. There are gaps in the acceptance due to the beam pipe (loss of 1.6% of the solid angle), the support legs (4.4% of the solid angle), and the cables (1.2% of the solid angle). Over nearly all of the acceptance, the amount of material that a particle has to traverse exceeds 1.3 m of iron equivalent.

The barrel portion of the muon chambers covers $|\cos\theta| < 0.68$ for four or more layers, and $|\cos\theta| < 0.72$ for one or more layers. It is constructed of 110 large area drift chambers, each of which is 1.2 m wide and 90 mm deep. The endcap muon chambers cover the range $0.67 < |\cos\theta| < 0.98$ and are constructed of four layers of streamer tubes placed perpendicular to the beam axis covering an area of $\approx 150 \text{ m}^2$.

Chapter 3

Measurement of the $\tau^- \rightarrow K^- \nu_\tau$ branching ratio

To determine the $\tau \rightarrow K \nu$ branching ratio relative to the $\tau \rightarrow \pi(K) \nu$ branching ratio (a quantity which will often be referred to in the text below as the *relative branching ratio*) a sample of 1242 $\tau \rightarrow \pi(K) \nu$ candidates was selected from 11381 $e^+ e^- \rightarrow \tau^+ \tau^-$ candidates, which in turn were selected from data taken at the OPAL detector at LEP during the years 1990 and 1991. Details of the selection of these and other event samples used in this thesis can be found in Appendix A or reference [14]. A momentum range was chosen where pion and kaon dE/dx were well separated. The events below a certain selection value in the dE/dx_{norm}^π distribution of the $\tau \rightarrow \pi(K) \nu$ sample were then selected as being $\tau \rightarrow K \nu$ candidates.

Since muons and pions have similar mass, they experience nearly the same energy loss as they traverse the central detector. The $\tau \rightarrow \mu \bar{\nu} \nu$ candidate sample was therefore used to estimate the pion contamination in the $\tau \rightarrow K \nu$ candidate sample. The Monte Carlo technique was used to determine the efficiencies for selecting $\tau \rightarrow K \nu$ out of the $\tau \rightarrow \pi(K) \nu$ candidate sample. The Monte Carlo technique involves using a computer program to simulate the production and all known decay modes of various species of particles and their passage through a detector. The events generated in this manner will be discussed in the next section along with a description of the formula and parameterisation used to calculate the predicted energy loss, dE/dx_{pred} , used in the calculation of normalised dE/dx according to equation 2.11.

3.1 Monte Carlo and the Predicted Mean Energy Loss

An accurate parameterisation for the mean energy loss was needed to calculate normalised dE/dx since it was this quantity which was used to differentiate between pions and kaons in the $\tau \rightarrow \pi(K)\nu$ sample to obtain the $\tau \rightarrow K\nu$ candidate sample.

Also required were Monte Carlo generated events to predict the efficiencies for selecting $\tau \rightarrow K\nu$ out of the $\tau \rightarrow \pi(K)\nu$ candidate sample. The following sections will describe the parameterisation of the mean energy loss and how it was used to generate the Monte Carlo events used in this measurement.

3.1.1 Parameterisation of the Predicted Mean Energy Loss

The predicted dE/dx of a particle of charge Qe (where e is the magnitude of the charge of an electron) traversing the OPAL jet chamber can be parameterized as follows [11]

$$dE/dx_{pred} = \frac{\xi Q^2}{\beta^2} \{ \kappa + \log(Q^2 \gamma^2) - \beta^2 \} \quad (3.12)$$

where

$$\kappa = \omega + \log \left(\frac{\beta^2 dE/dx_{pred}}{Q^2} \right) \quad (3.13)$$

Equation 3.12 is essentially a modified Bethe-Bloch equation (see for comparison equation 2.6) parameterised with two constants ξ and ω which are dependent upon the state and composition of the gas used in the OPAL jet chamber. Both κ and ω are dimensionless quantities, but since the logarithmic term in equation 3.13 is not, quoted values of ω in this thesis are given under the assumption that the dE/dx appearing in equations 3.12 and 3.13 is given in keV/cm. The density effect is not included in this parameterisation since we are interested in a momentum region where the density effect is negligible for pions, muons, and kaons.

In order to achieve a well understood background determination in the relative branching ratio measurement, the chosen parameterisation of the energy loss must describe both pion and muon energy loss in the momentum range of interest. Of equal importance, however, is that the energy loss parameterisation also describe kaon energy loss since we rely entirely upon the energy loss parameterisation to predict the efficiencies in the calculation of the branching ratio.

Thus, to determine the constants ξ and ω used in the parameterisation, we would like to fit to a data sample composed of significant numbers of pions, kaons, and muons.

To achieve this, a maximum likelihood fit was performed simultaneously to the dE/dx_{meas} of two data samples. The first sample was obtained from the $\tau \rightarrow \mu \bar{\nu} \nu$ candidate sample (which was selected according the criteria found in appendix A) as follows:

1. Only events in the momentum range between 3.5 to 20 GeV/c were considered. This momentum range was chosen since it was the one over which the branching ratio measurement was finally performed (pion and kaon dE/dx are well separated below 20 GeV/c and the momentum threshold in the lab frame for kaon production in $\tau \rightarrow K \nu$ decays is 3.5 GeV/c).
2. Only events with local ϕ (ϕ within one of the 24 jet chamber anode cells) *not* between 6.5° to 8.5° were considered. This requirement was made to remove the region around the anode plane (local $\phi = 7.5^\circ$) in each jet chamber cell in order to ensure well understood dE/dx_{meas} and $\sigma(dE/dx)$ for each event.
3. Only events with $N_{dE/dx} > 130$ were considered, again to ensure well understood dE/dx_{meas} and $\sigma(dE/dx)$ for each event.

After all requirements, there remained 1858 candidates which consisted of approximately 98% muons with a 2% pion contamination as estimated from the Monte Carlo generated event sample.

The second sample was obtained from the $e^+e^- \rightarrow \tau^+\tau^-$ candidate sample in the

following fashion:

1. Most electrons were removed from the sample by requiring that the event *not* be identified as a $\tau \rightarrow e \bar{\nu} \nu$ candidate.
2. Most muons were removed by requiring that the event *not* be identified as a $\tau \rightarrow \mu \bar{\nu} \nu$ candidate. This requirement was made to make this second data sample independent from the first.
3. The data sample was made independent from the $\tau \rightarrow \pi(K) \nu$ candidate sample by requiring that the event *not* be identified as a $\tau \rightarrow \pi(K) \nu$ candidate.
4. Only events in the momentum range between 3.5 to 20 GeV/c were considered.
5. Only events with local ϕ *not* between 6.5° to 8.5° were considered.
6. Only events with $N_{dE/dx} > 130$ were considered.

After all requirements there remained 5313 candidates which consisted of approximately 85% pions, 3% to 4% kaons, and about 5% each of muons and electrons as estimated from the Monte Carlo generated event sample.

Parameters of the maximum likelihood fit were ξ and ω , the constant A used in the calculation of $\sigma(dE/dx)$ according to equation 2.4, and the relative fractions of kaons, muons, and electrons in the second data sample. The fractions of muons and pions in the first sample were held fixed at the values determined in reference [14] (ie; 98% and 2%, respectively).

In order to obtain a numerical solution to the transcendental equation for κ formed by equations 3.12 and 3.13 an iterative approach was used using the energy loss parameterisation described in reference [11] as the first guess to be used in equation 3.13. It was found that three iterations were more than sufficient to ensure convergence to a solution. As an aside it should be mentioned that the energy loss parameterisation found in reference [11]

Parameter	Value
ξ	0.306 ± 0.003 keV/cm
ω	19.26 ± 0.01

Table 3.1: The two predicted energy loss parameters determined from a maximum likelihood fit to the measured energy loss (in keV/cm) of data samples derived from the $e^+e^- \rightarrow \tau^+\tau^-$ candidate sample.

was not used in this analysis since it was found not to provide an optimal description of kaon energy loss in the momentum range of interest.

In other analyses, it has been customary to ignore the dependence of κ upon $\ln(\beta^2 dE/dx_{pred})$ and instead assume κ is a constant in order to simplify the parameterisation and also make individual calculations of dE/dx_{pred} on an event-by-event basis faster [11]. However the assumption that $\ln(\beta^2 dE/dx_{pred})$ is constant is only appropriate in the region where dE/dx falls as $1/\beta^2$ thus making $\beta^2 dE/dx$ equal to a constant, and the high momentum region where β^2 essentially equals one and dE/dx is essentially constant due to the Fermi plateau effect. At intermediate momenta, however, $\ln(\beta^2 dE/dx_{pred})$ is not constant and although the dependence of κ upon changes in $\beta^2 dE/dx$ is weak over this momentum range, it still exists and is non-negligible.

Since this is the momentum range of interest to this analysis and since the data samples used in this analysis are not large enough to make the iterative approach to solving equations 3.12 and 3.13 prohibitively time consuming, it was decided to include the $\ln(\beta^2 dE/dx_{pred})$ term in the determination of the dE/dx_{pred} parameterisation used in this analysis. The dE/dx gas parameters determined by the fit are found in table 3.1.

Figure 3.10 (a) shows a plot of dE/dx_{meas} versus dE/dx_{pred} for the $\tau \rightarrow \mu \bar{\nu} \nu$ sample. Note that the slope of the graph is consistent with one and the intercept is consistent

with zero, as would be expected if dE/dx_{pred} were predicting the data ionization energy loss correctly. Figure 3.10 (b) shows a plot of $dE/dx_{meas} - dE/dx_{pred}$ versus momentum for the $\tau \rightarrow \mu \bar{\nu} \nu$ candidate sample. Note that the line fitted to the plot has both slope and intercept consistent with zero, again as would be expected if dE/dx_{pred} were modelling dE/dx_{meas} correctly.

As mentioned earlier, it is of vital importance that the chosen parameterisation describes the energy loss of kaons as well as that of muons and pions. In order to estimate how well dE/dx_{pred} predicts the ionization energy loss of kaons, a rough sample of kaons was obtained from the $e^+e^- \rightarrow \tau^+\tau^-$ sample in the following fashion:

1. Only events in the barrel with $N_{dE/dx} > 130$, momentum between 3.5 to 20 GeV/c, and one charged track per jet cone were considered. The momentum range was chosen to give the best possible separation between pions and kaons without compromising the statistics of the sample.
2. Events classified as either $\tau \rightarrow \mu \bar{\nu} \nu$ or $\tau \rightarrow e \bar{\nu} \nu$ were *rejected*.
3. The dE/dx of the remaining events was normalised to pion dE/dx and then all events with $dE/dx_{norm}^\pi > -1.0$ were rejected. This effectively removed about 85% of the pions, all of the remaining electrons, and virtually all of the remaining muons. The value of $dE/dx_{norm}^\pi > -1.0$ was chosen to eliminate as many pions as possible without seriously biasing the kaon sample. It was found by examining the Monte Carlo generated events that this value, in conjunction with the momentum range used, yielded no perceptible biasing of the kaons.
4. The events surviving this selection were then normalised to kaon dE/dx . Most of the few remaining pions were then removed from the upper portion of this distribution using Monte Carlo generated events to perform the background subtraction. The remaining events were mostly kaons with some pions in the sample which contaminate the upper portion of the distribution. The lower portion of the distribution is virtually pure kaons.

A plot of the dE/dx_{norm}^K of the rough sample of kaons thus obtained is shown in figure

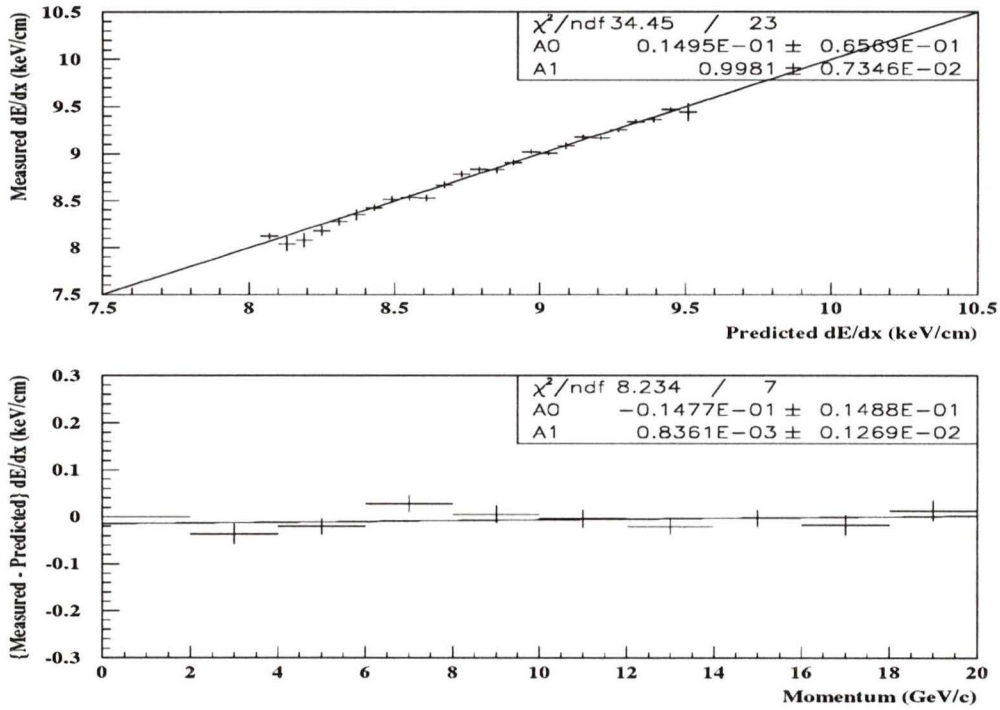


Figure 3.10: (a) dE/dx_{meas} versus dE/dx_{pred} for the data $\tau \rightarrow \mu \bar{\nu}$ candidate sample between 3.5 to 20 GeV/c. Note that the slope, $A1$, is consistent with one and the intercept, $A0$, is consistent with zero, as would be expected if dE/dx_{pred} was predicting the muon energy loss correctly.

(b) $(dE/dx_{meas} - dE/dx_{pred})$ versus momentum for the $\tau \rightarrow \mu \bar{\nu}$ candidate sample between 3.5 to 20 GeV/c. Note the slope and intercept of the fitted line are both consistent with zero, again indicating that dE/dx_{pred} is modelling the data well.

3.11. Note that the mean is consistent zero and the width is consistent with one, which demonstrates that the parameterisation appears to adequately describe the energy loss of kaons in the momentum range of interest. The Gaussian fit was not performed to the data points above $dE/dx_{norm}^K = 1.0$ since studies of Monte Carlo generated events suggest that these are almost certainly background pion events which remain after the background subtraction procedure described above.

3.1.2 Monte Carlo

The computer program KORALZ3.8 was used to simulate the production and all known decay modes of τ leptons to generate a sample of momentum four-vectors. The GEANT computer program then used these four-vectors as input to simulate the passage of the particles through the OPAL detector [13], resulting in a Monte Carlo generated sample of 72000 simulated τ pair events. It was found that the angular and momentum distributions of the Monte Carlo generated particles produced in this fashion simulated the data well (see examples in figure 3.12). It was found, however, that the energy loss simulation of the standard Monte Carlo generated events was not sufficiently precise for the purposes of this analysis. The number of jet chamber hits, $N_{dE/dx}$, used in the truncated mean calculation of dE/dx was also not correctly simulated.

To correct the Monte Carlo generated events, new dE/dx and $N_{dE/dx}$ for each track were obtained in the following fashion:

1. The $N_{dE/dx}$ problem was corrected by randomly sampling $N_{dE/dx}$ probability distributions obtained from τ decay events in the $e^+e^- \rightarrow \tau^+\tau^-$ data sample which only contained one charged track. It was found, however, that the data $N_{dE/dx}$ distributions depended both upon the local ϕ coordinate within one of the 24 anode cells in the jet chamber, and momentum (see examples in figure 3.13). A dedicated study showed that $N_{dE/dx}$ distributions in five bins in local ϕ (0° to 3° ; ...; 12° to 15°), and three bins of momentum (2 to 5 GeV/c; 5 to 20 GeV/c; 20 GeV/c and up), were sufficient

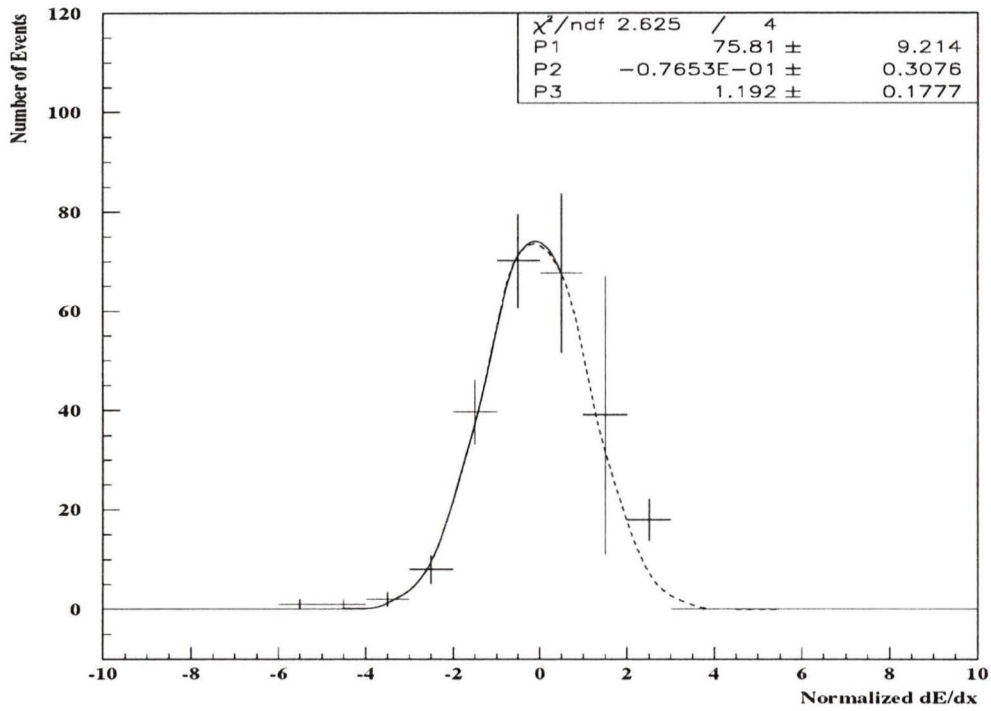


Figure 3.11: dE/dx_{norm}^K of the rough kaon sample (normalized to kaon dE/dx using dE/dx_{pred} with the kaon mass and the parameters obtained from the fit). Note that the mean is consistent with zero and the width is close to one as would be expected if dE/dx_{pred} was predicting kaon dE/dx well.

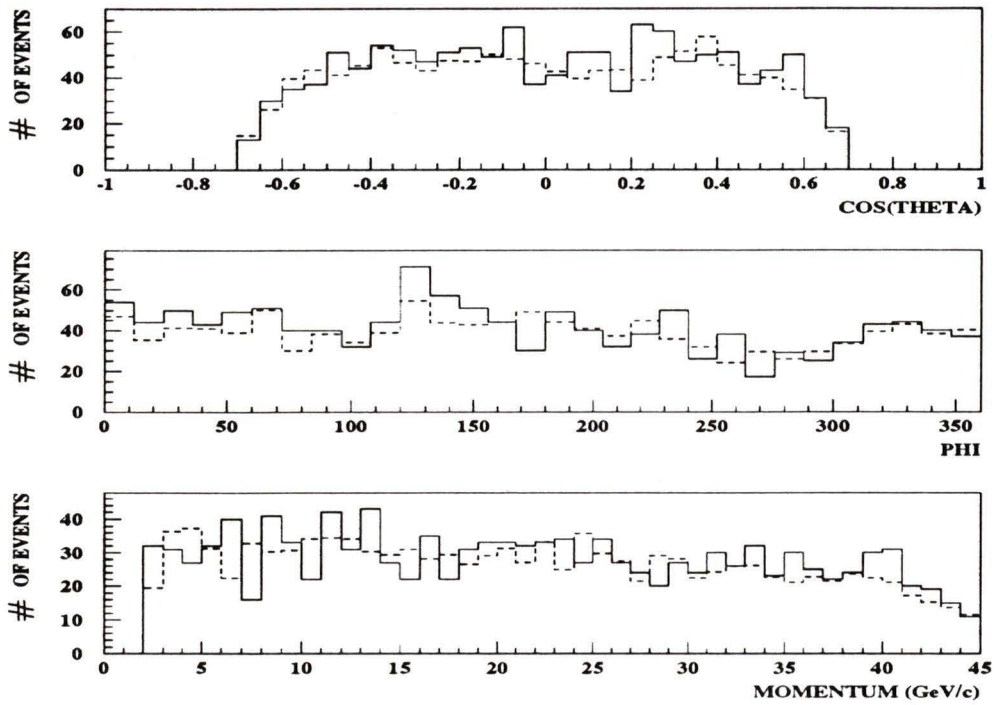


Figure 3.12: (a) Distribution in $\cos \theta$ for data (solid line) and Monte Carlo (dashed line) generated $\tau \rightarrow \mu \bar{\nu} \nu$ candidate samples.

(b) Distribution in ϕ for data (solid line) and Monte Carlo (dashed line) generated $\tau \rightarrow \mu \bar{\nu} \nu$ candidate samples.

(c) Momentum distribution for data (solid line) and Monte Carlo (dashed line) generated $\tau \rightarrow \mu \bar{\nu} \nu$ candidate samples.

$\tau \rightarrow e \bar{\nu} \nu$ and $\tau \rightarrow \pi(K) \nu$ samples show similar agreement between data and Monte Carlo generated events.

to describe the data adequately. Thus 15 probability distributions were formed based upon these $N_{dE/dx}$ distributions. The $N_{dE/dx}$ value for a particular Monte Carlo generated track was then obtained by randomly sampling the $N_{dE/dx}$ probability distribution appropriate to the track's momentum and direction in local ϕ .

2. The predicted dE/dx for each track, dE/dx_{pred} , was calculated using equations 3.12 and 3.13 with the Monte Carlo generated momentum and mass, and the predicted energy loss parameters derived from the data as described in the previous section.
3. The uncertainty on the dE/dx of the track, $\sigma(dE/dx)$, was calculated using equation 2.4. Namely,

$$\sigma(dE/dx) = A \cdot (N_{dE/dx})^{-0.43} \cdot dE/dx_{pred}.$$

4. $\sigma(dE/dx)$ and dE/dx_{pred} were then used to calculate the new dE/dx of the Monte Carlo generated particle as follows:

$$dE/dx = dE/dx_{pred} + G \cdot \sigma(dE/dx)$$

where G was a number randomly sampled from a normal Gaussian distribution.

Figure 3.14 shows the normalized dE/dx distributions for the data and Monte Carlo generated $\tau \rightarrow \mu \bar{\nu} \nu$ and $\tau \rightarrow \pi(K) \nu$ candidate samples in the momentum range of interest to this analysis. In each case the data distributions are well simulated by the Monte Carlo generated events.

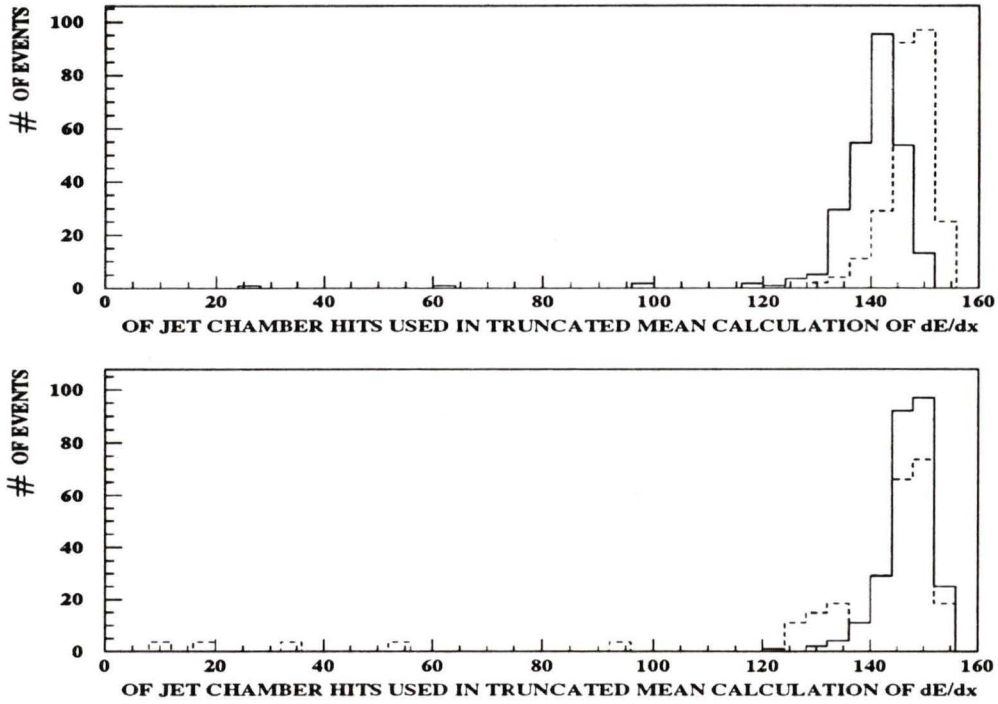


Figure 3.13: (a) $N_{dE/dx}$ distribution for data $\tau \rightarrow \mu \bar{\nu} \nu$ candidate sample with local ϕ between 0° to 3° (solid line) and 9° to 12° (dashed line). In both cases the momentum is between 20 to 45 GeV/c.

(b) $N_{dE/dx}$ distribution for data $\tau \rightarrow \mu \bar{\nu} \nu$ candidate sample with momentum between 20 to 45 GeV/c (solid line) and 2 to 5 GeV/c (dashed line). In both cases local ϕ is between 9° to 12° .

For presentation purposes all histograms have been normalised such that the area under each histogram is equal to one.

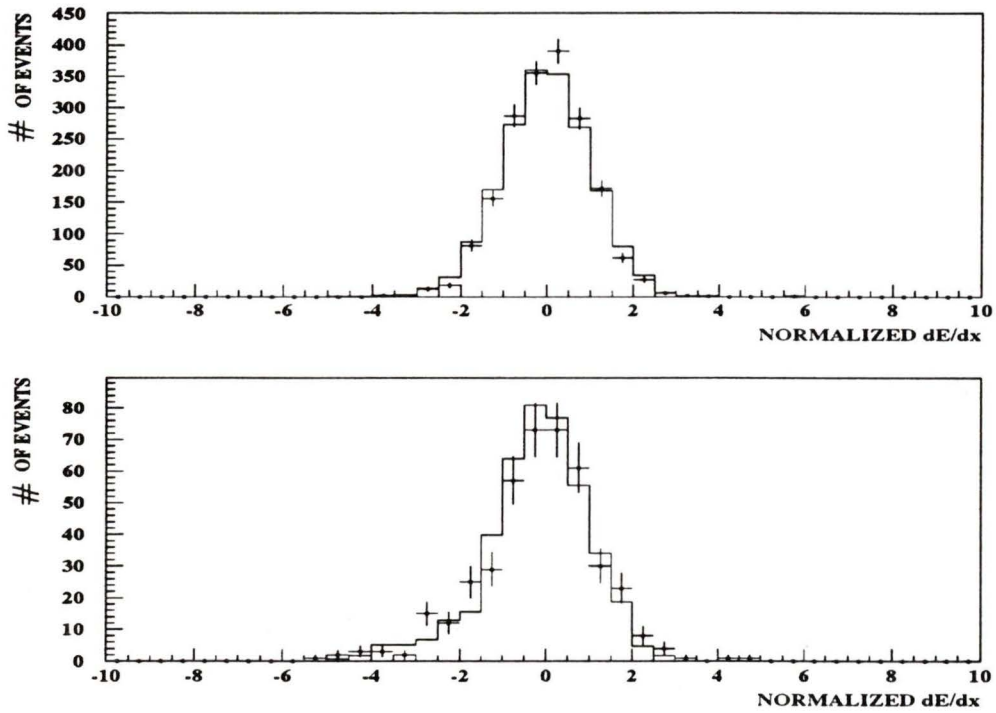


Figure 3.14: (a) Normalized dE/dx distribution for the $\tau \rightarrow \mu \bar{\nu}$ candidate sample between 3.5 to 20 GeV/c for both the data (points) and the Monte Carlo generated events (histogram). (b) Normalized dE/dx distribution for the $\tau \rightarrow \pi(K) \nu$ candidate sample between 3.5 to 20 GeV/c for both the data (points) and the Monte Carlo generated events (histogram).

3.2 Calculation of the $\tau^- \rightarrow K^- \nu_\tau$ Relative Branching Ratio

The branching ratio measurement was performed using the following steps:

1. A momentum range was chosen where the pions and kaons in the dE/dx_{norm}^π distribution of the $\tau \rightarrow \pi(K)\nu$ candidate sample were well separated.
2. $\tau \rightarrow K\nu$ candidates were selected by choosing events below a certain value of dE/dx_{norm}^π in this distribution. This dE/dx_{norm}^π value will be referred to as the dE/dx_{norm}^π selection value or the selection value in dE/dx_{norm}^π . The pion background in this $\tau \rightarrow K\nu$ sample was estimated using the dE/dx_{norm}^μ distribution of the $\tau \rightarrow \mu\bar{\nu}\nu$ sample.

The dE/dx resolving power, D , for various particles in the OPAL jet chamber is shown in figure 2.9. Notice that the best separation between the energy loss measurements for pions and kaons occurs for momenta less than about 20 GeV/c and therefore this was taken as the upper limit on the momentum range for $\tau \rightarrow K\nu$ candidates in this measurement. The momentum threshold in the lab frame for kaons in $\tau \rightarrow K\nu$ decays is about 3.5 GeV/c and therefore this was chosen as the lower bound on the momentum range. Figure 3.15 shows the momentum distribution for both the data and Monte Carlo generated $\tau^- \rightarrow \pi^-(K^-)\nu_\tau$ candidate samples. Dotted lines denote the momentum range of interest.

The selection value in dE/dx_{norm}^π was chosen such that the following requirements were met:

1. The pion background in the $\tau \rightarrow K\nu$ candidate sample was low.
2. The efficiency for selecting $\tau \rightarrow K\nu$ events out of the $\tau \rightarrow \pi(K)\nu$ sample in the chosen momentum range was high.

If we examine figure 3.16 we see that if the dE/dx_{norm}^π selection value is chosen as -3.0

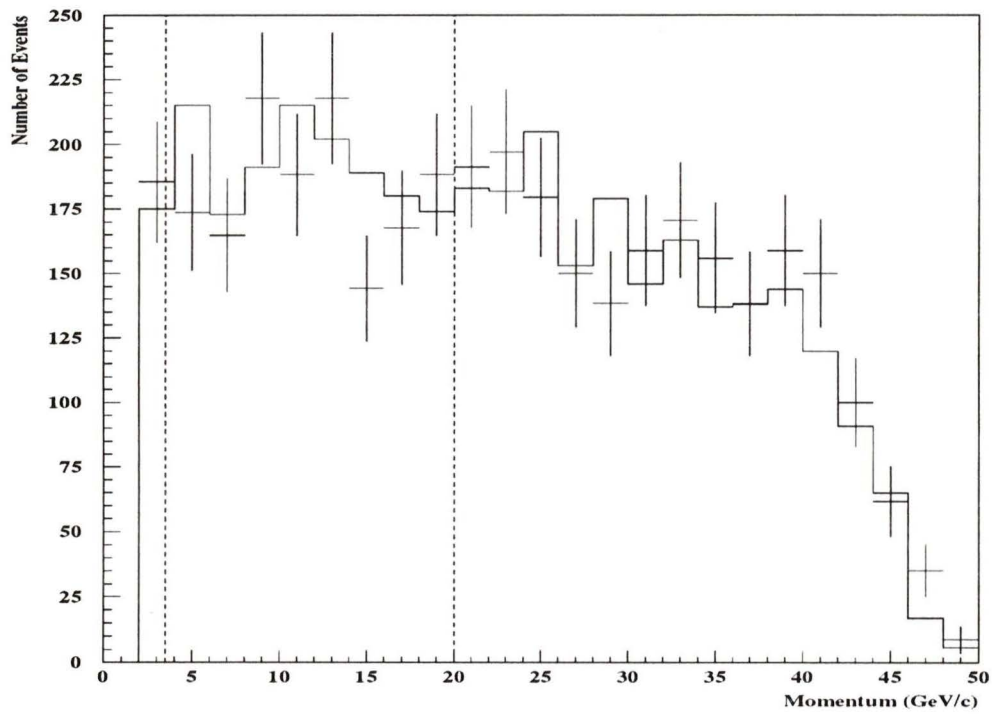


Figure 3.15: Momentum distribution of the $\tau \rightarrow \pi(K) \nu$ candidate sample for both the data (points) and Monte Carlo generated events (histogram). Dotted lines denote the momentum range in which $\tau \rightarrow K \nu$ candidates were selected out of the $\tau \rightarrow \pi(K) \nu$ sample.

-3.0 (meaning that all events below dE/dx_{norm}^π equal to negative three are selected as $\tau \rightarrow K \nu$ candidates), the background is very low (about 3%), but the efficiency is also low (around 45%). A dE/dx_{norm}^π selection value of -2.0 yields a higher efficiency (around 80%) but the background is high (around 20%). Thus the selection value was chosen to be -2.5; the background was reasonably low (around 10%), and the efficiency was acceptably high (around 65%). Figure 3.17 shows the $\tau \rightarrow \pi(K) \nu$ normalised energy loss distribution for both the data and the Monte Carlo generated events. An expanded view of the portion of this distribution that was selected as $\tau \rightarrow K \nu$ candidates is seen in figure 3.18.

To obtain a well understood uncertainty in dE/dx , the number of jet chamber hits used in the calculation of mean energy loss, $N_{dE/dx}$, was required to be at least 130, and events with local ϕ along the anode plane were excluded by requiring that local ϕ *not* be between 6.5° to 8.5° .

With the chosen selection value in the dE/dx_{norm}^π distribution of the $\tau \rightarrow \pi(K) \nu$ candidate sample we can calculate the $\tau \rightarrow K \nu$ branching ratio relative to the $\tau \rightarrow \pi(K) \nu$ branching ratio according to the following formula:

$$\frac{\Gamma(\tau \rightarrow K \nu)}{\Gamma(\tau \rightarrow \pi(K) \nu)} = \frac{N_{cand}^{\tau \rightarrow K \nu}}{N_{cand}^{\tau \rightarrow \pi(K) \nu}} \cdot \frac{(1 - f_{bkgd}^{non-K})}{(1 - f_{bkgd}^{non-\pi, K})} \cdot \frac{1}{\epsilon^{\tau \rightarrow K \nu}} \cdot \frac{1}{F_{bias}^{\tau \rightarrow K \nu}} \quad (3.14)$$

where $N_{cand}^{\tau \rightarrow K \nu}$ is the number of $\tau \rightarrow K \nu$ candidates below the selection value in the normalised energy loss distribution of the $\tau \rightarrow \pi(K) \nu$ sample between 3.5 to 20.0 GeV/c, and $N_{cand}^{\tau \rightarrow \pi(K) \nu}$ is the number of events in the $\tau \rightarrow \pi(K) \nu$ sample *before* the momentum selection. The quantity f_{bkgd}^{non-K} is the estimated background fraction in the $\tau \rightarrow K \nu$ candidate sample from other τ decay modes, and $f_{bkgd}^{non-\pi, K}$ is the estimated background fraction in the $\tau \rightarrow \pi(K) \nu$ candidate sample from other τ decay modes and non τ sources. The quantity $\epsilon^{\tau \rightarrow K \nu}$ is the estimated efficiency for selecting $\tau \rightarrow K \nu$ events out of the total number of $\tau \rightarrow K \nu$ events in the $\tau \rightarrow \pi(K) \nu$ candidate sample over the *entire* momentum range (note that this is different than the efficiency, shown in figure 3.16, for selecting $\tau \rightarrow K \nu$ events out of the $\tau \rightarrow \pi(K) \nu$ sample in the chosen momentum range), and $F_{bias}^{\tau \rightarrow K \nu}$ is the relative enhancement of $\tau \rightarrow K \nu$ decays in the $\tau \rightarrow \pi(K) \nu$ sample introduced by any biases in the preselection procedure for the $\tau \rightarrow \pi(K) \nu$ sample.

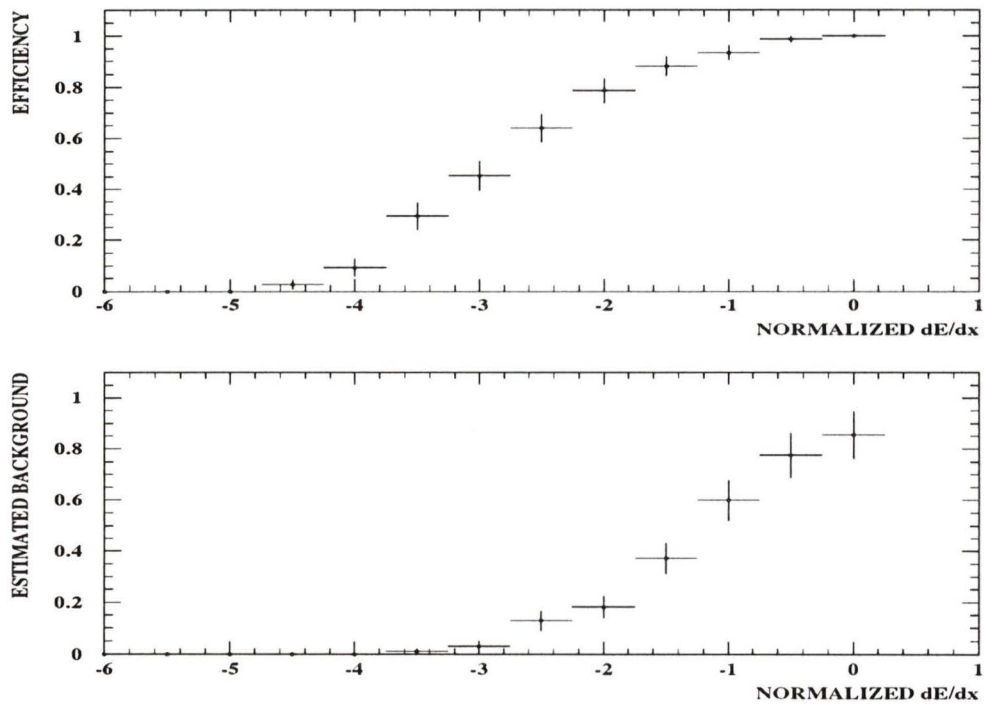


Figure 3.16: (a) Efficiency for selecting $\tau \rightarrow K \nu$ events out of the $\tau \rightarrow \pi(K) \nu$ candidate sample (after the momentum selection) as a function of the selection value in normalised dE/dx . (b) Estimated background in the $\tau \rightarrow K \nu$ candidate sample as a function of the selection value in normalised dE/dx .

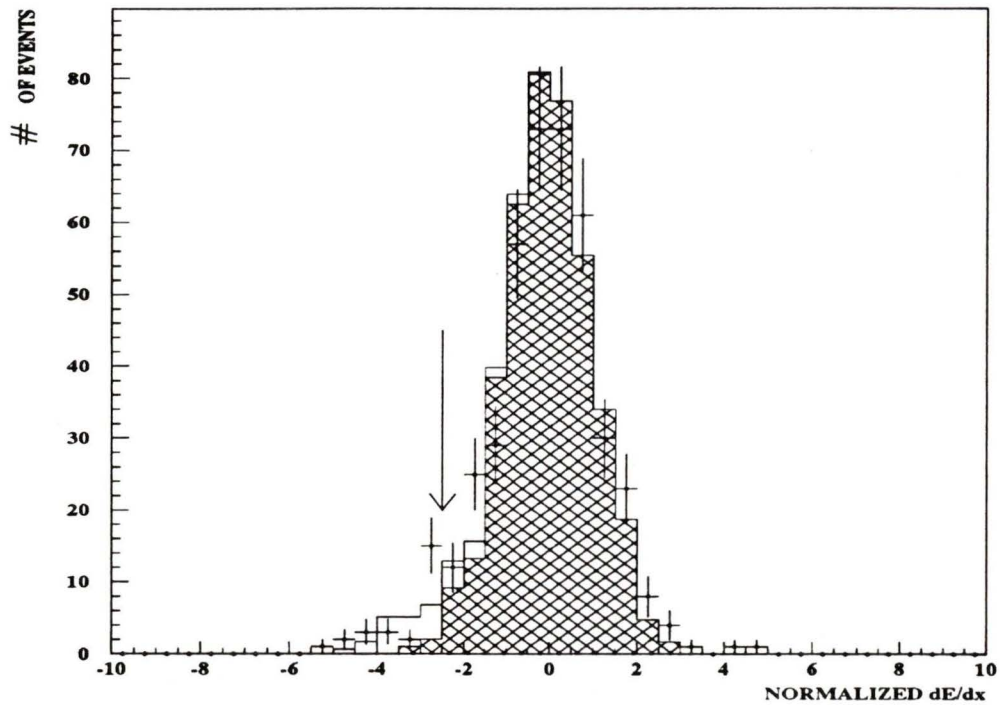


Figure 3.17: Energy loss distribution of the $\tau \rightarrow \pi(K)\nu$ candidate sample normalized to a pion hypothesis for both the data (points) and Monte Carlo generated events (histogram). The shaded portion of the histogram represents the non $\tau \rightarrow K\nu$ events in the Monte Carlo generated $\tau \rightarrow \pi(K)\nu$ candidate sample. All events below the normalized energy loss selection value denoted by the arrow were selected as $\tau \rightarrow K\nu$ candidates.

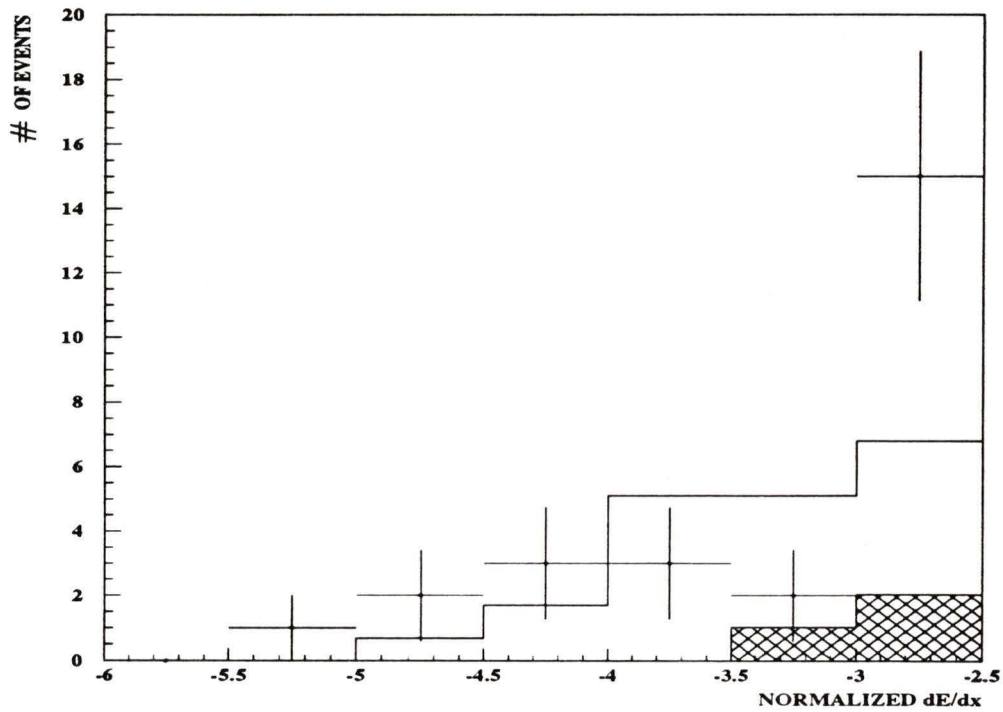


Figure 3.18: Energy loss distribution of the $\tau \rightarrow K \nu$ candidate sample normalized to a pion hypothesis for both the data (points) and Monte Carlo generated events (histogram). The shaded portion of the histogram represents the non $\tau \rightarrow K \nu$ events in the Monte Carlo generated $\tau \rightarrow K \nu$ candidate sample.

Both $N_{cand}^{\tau \rightarrow K \nu}$ and $N_{cand}^{\tau \rightarrow \pi(K) \nu}$ are obtained directly from the data. $f_{bkgd}^{non-\pi, K}$ has been previously determined to be [14]:

$$f_{bkgd}^{non-h} = (7.6 \pm 0.7)\%.$$

The quantities $\epsilon^{\tau \rightarrow K \nu}$ and $F_{bias}^{\tau \rightarrow K \nu}$ were both estimated from the Monte Carlo generated events.

The parameter f_{bkgd}^{non-K} was estimated using both the data $\tau \rightarrow \mu \bar{\nu} \nu$ sample and Monte Carlo generated events. The data $\tau \rightarrow \mu \bar{\nu} \nu$ sample (which is nearly pure muons with only a small pion contamination) was used to predict the pion background fraction in the $\tau \rightarrow K \nu$ candidate to be 0.093 ± 0.031 , and Monte Carlo generated events were used to predict the contamination in the $\tau \rightarrow K \nu$ candidate sample from kaons which didn't result from $\tau \rightarrow K \nu$. The dominant source of such events were $\tau^- \rightarrow K^* \nu_\tau$ decays where the K^* promptly decayed to a charged kaon and a neutral pion. The background fraction in the $\tau \rightarrow K \nu$ sample due to this process was estimated to be 0.035 ± 0.024 where the dominant source of uncertainty was Monte Carlo statistics and where a branching ratio of $Br(\tau \rightarrow K^* \nu) = 0.0047 \pm 0.0002$ was assumed in the Monte Carlo generation of events.

The above procedure determined the central value of the relative branching ratio to be:

$$\frac{\Gamma(\tau \rightarrow K \nu)}{\Gamma(\tau \rightarrow \pi(K) \nu)} = 0.087 \pm 0.017$$

where only the statistical error is quoted at this point. Values and uncertainties of the parameters used to calculate the branching ratio via equation 3.14 are seen in tables 3.2, 3.3, and 3.4.

3.2.1 Evaluation of the systematic errors

The systematic studies are shown in table 3.5. The upper and lower limits of the momentum range were varied by 0.5 GeV/c to test the branching ratio sensitivity to the

Parameter	Value corresponding to selection value of $dE/dx_{norm}^\pi < -2.5$
f_{bkgd}^{non-K}	0.128 ± 0.039
$f_{bkgd}^{non-\pi,K}$	0.076 ± 0.007
$\epsilon^{\tau \rightarrow K\nu}$	0.273 ± 0.034
$F_{bias}^{\tau \rightarrow K\nu}$	0.988 ± 0.072
$\epsilon^{\tau \rightarrow K\nu} * F_{bias}^{\tau \rightarrow K\nu}$ ^a	0.270 ± 0.039

^a $\epsilon^{\tau \rightarrow K\nu}$ and $F_{bias}^{\tau \rightarrow K\nu}$ are correlated and thus used in the calculation as a combined quantity.

Table 3.2: Parameters used in the calculation of the $\tau^- \rightarrow K^- \nu_\tau$ relative branching ratio.

	# of MC Events
$\tau \rightarrow \pi(K)\nu$ events before any selection	16656
$\tau \rightarrow K\nu$ events before any selection	1097
$\tau \rightarrow \pi\nu$ events in $\tau \rightarrow \pi(K)\nu$ candidate sample in entire momentum range ^a	2527
$\tau \rightarrow K\nu$ events in $\tau \rightarrow \pi(K)\nu$ candidate sample in entire momentum range ^a	176
$\tau \rightarrow \pi\nu$ events in $\tau \rightarrow \pi(K)\nu$ candidate sample between 3.5 to 20 GeV/c	1092
$\tau \rightarrow K\nu$ in $\tau \rightarrow \pi(K)\nu$ candidate sample between 3.5 to 20 GeV/c	75
$\tau \rightarrow K\nu$ in selected $\tau \rightarrow K\nu$ candidate sample	48

^aafter local ϕ and $N_{dE/dx}$ selections.

Table 3.3: Monte Carlo generated events used in the calculation of the $\tau^- \rightarrow K^- \nu_\tau$ relative branching ratio.

	Number of Data Events
$\tau \rightarrow \pi(K)\nu$ candidates before any other selection	1242
$\tau \rightarrow \pi(K)\nu$ candidates in entire momentum range ^a	1045
$\tau \rightarrow \pi(K)\nu$ candidate events between 3.5 to 20 GeV/c	424
$\tau \rightarrow K\nu$ selected candidates	26

^aafter local ϕ and $N_{dE/dx}$ selections.

Table 3.4: Data event parameters used in the calculation of the $\tau^- \rightarrow K^- \nu_\tau$ relative branching ratio.

momentum range used. The energy loss resolution was also varied within its uncertainty to test the branching ratio dependence.

The selection value in $N_{dE/dx}$ was varied from 130 down to 40 and the selection values in local ϕ were changed to exclude a region of 3° around the anode plane as opposed to the original exclusion of only 2° . Finally, the parameters used to calculate dE/dx_{pred} were varied within their uncertainties to examine how this affected the branching ratio.

The changes in the relative branching ratio induced by these variations are quantified by the systematic errors seen in table 3.5. Adding these errors in quadrature with the combined uncertainties in $\epsilon^{\tau \rightarrow K\nu}$, $F_{bias}^{\tau \rightarrow K\nu}$, f_{bkgd}^{non-K} , and $f_{bkgd}^{non-\pi,K}$ yields

$$\frac{\Gamma(\tau \rightarrow K\nu)}{\Gamma(\tau \rightarrow \pi(K)\nu)} = 0.087 \pm 0.017_{-0.017}^{+0.016}$$

where the first uncertainty is statistical and the second is systematic.

A comparison of the relative branching ratio corresponding to the dE/dx_{norm}^π selection value of -2.5 to those corresponding to the selection values of -2.0 and -3.0 is seen in table 3.6. The large errors on the relative branching ratios corresponding to the selection values of -2.0 and -3.0 are predominantly from the variation of ξ within one

SYSTEMATIC	difference in relative BR	
	-	+
momentum 3.5 to 19.5 GeV/c		0.002
momentum 3.5 to 20.5 GeV/c		0.002
momentum 3.0 to 20 GeV/c		0.002
momentum 4.0 to 20 GeV/c	0.003	
resolution $+\sigma_{RES}$		0.004
resolution $-\sigma_{RES}$	0.002	
$N_{dE/dx} > 40$		0.003
local ϕ not between 6° to 9°	0.005	
$\xi + \sigma_\xi$		0.008
$\xi - \sigma_\xi$	0.009	
$\omega + \sigma_\omega$	< 0.001	< 0.001
$\omega - \sigma_\omega$	< 0.001	< 0.001
$\epsilon^{\tau \rightarrow K\nu} * F_{bias}^{\tau \rightarrow K\nu}$ uncertainty ^a	0.013	0.013
f_{bkgd}^{non-K} uncertainty ^b	0.004	0.004
$f_{bkgd}^{non-\pi,K}$ uncertainty ^b	< 0.001	< 0.001
TOTAL	0.017	0.016

^aError results from Monte Carlo generated event sample statistical uncertainties.

^bError results from both data and Monte Carlo generated event sample statistical uncertainties.

Table 3.5: Change in the $\tau^- \rightarrow K^- \nu_\tau$ relative branching ratio as a function of various systematic studies.

Selection Value	Relative BR	$N_{cand}^{\tau \rightarrow K \nu}$	ϵ^a	f_{bkgd}^{non-K}
$dE/dx_{norm}^\pi < -3.0$	$0.058 \pm 0.018_{-0.013}^{+0.068}$	11	0.453 ± 0.057	0.030 ± 0.020
$dE/dx_{norm}^\pi < -2.5$	$0.087 \pm 0.017_{-0.017}^{+0.016}$	26	0.640 ± 0.055	0.128 ± 0.039
$dE/dx_{norm}^\pi < -2.0$	$0.097 \pm 0.014_{-0.026}^{+0.033}$	38	0.787 ± 0.047	0.182 ± 0.042

^aEfficiency for selecting $\tau \rightarrow K \nu$ events out of the $\tau \rightarrow \pi(K) \nu$ candidate sample between 3.5 to 20 GeV/c.

Table 3.6: A comparison of the relative branching ratios, number of $\tau^- \rightarrow K^- \nu_\tau$ candidate events, efficiencies, and estimated backgrounds corresponding to three different selection values in dE/dx_{norm}^π .

σ of its central value; this causes a large change in the position of the peaks in the $\tau^- \rightarrow \pi^- (K^-) \nu_\tau$ dE/dx_{norm}^π distribution, resulting in badly understood efficiencies and backgrounds. As mentioned above, the dE/dx_{norm}^π selection values of -3.0 and -2.0 were rejected specifically because of their respective sensitivity to badly understood efficiencies and backgrounds.

Chapter 4

Discussion of the results

A phenomenological prediction of the $\tau \rightarrow K\nu$ relative branching ratio can be calculated from the decay widths corresponding to $\tau \rightarrow \pi\nu$ and $\tau \rightarrow K\nu$ decays, given by the expressions [8]

$$\Gamma(\tau \rightarrow \pi\nu) = \frac{G^2 f_\pi^2 \cos^2 \theta_C m_\tau^3}{16\pi} \left[1 - \frac{m_\pi^2}{m_\tau^2} \right]^2 \quad (4.15)$$

and

$$\Gamma(\tau \rightarrow K\nu) = \frac{G^2 f_K^2 \sin^2 \theta_C m_\tau^3}{16\pi} \left[1 - \frac{m_K^2}{m_\tau^2} \right]^2 \quad (4.16)$$

where G^2 is the Fermi coupling constant, θ_C is the Cabibbo angle, and f_π and f_K are factors which take into account the fact that the quark decay products are not free but rather bound into a hadronic final state. Taking the ratio of equations 4.15 and 4.16 yields the following prediction for the $\tau^- \rightarrow K^- \nu_\tau$ relative branching ratio

$$\frac{\Gamma(\tau \rightarrow K\nu)}{\Gamma(\tau \rightarrow \pi\nu)} = \tan^2 \theta_C \frac{f_K}{f_\pi} \left[\frac{m_\tau^2 - m_K^2}{m_\tau^2 - m_\pi^2} \right]. \quad (4.17)$$

Theory does not predict the values of θ_C , f_π , and f_K , but they can be obtained from the branching ratios of the decays $K^- \rightarrow \mu^- \bar{\nu}_\mu$ and $\pi^- \rightarrow \mu^- \bar{\nu}_\mu$ since

$$Br(\pi \rightarrow \mu\nu) = \frac{G^2 f_\pi^2 \cos^2 \theta_C m_\pi m_\mu^2 \tau_\pi}{8\pi\hbar} \left[1 - \frac{m_\mu^2}{m_\pi^2} \right]^2 \quad (4.18)$$

and

$$Br(K \rightarrow \mu\nu) = \frac{G^2 f_K^2 \sin^2 \theta_C m_K m_\mu^2 \tau_K}{8\pi\hbar} \left[1 - \frac{m_\mu^2}{m_K^2} \right]^2 \quad (4.19)$$

where τ_π and τ_K are the lifetimes of the pion and kaon, respectively. Taking the ratio of equations 4.18 and 4.19 then yields:

$$\frac{Br(K \rightarrow \mu\nu)}{Br(\pi \rightarrow \mu\nu)} = \tan^2 \theta_C \frac{f_K^2 m_\pi^3 \tau_K}{f_\pi^2 m_K^3 \tau_\pi} \frac{[m_K^2 - m_\mu^2]^2}{[m_\pi^2 - m_\mu^2]^2} \quad (4.20)$$

which, when combined with equation 4.17, yields

$$\frac{\Gamma(\tau \rightarrow K\nu)}{\Gamma(\tau \rightarrow \pi\nu)} = \frac{m_K^3 \tau_\pi (m_\tau^2 - m_K^2)^2 (m_\pi^2 - m_\mu^2)^2}{m_\pi^3 \tau_K (m_\tau^2 - m_\pi^2)^2 (m_K^2 - m_\mu^2)^2} \frac{Br(K \rightarrow \mu\nu)}{Br(\pi \rightarrow \mu\nu)}$$

which yields the prediction

$$\frac{\Gamma(\tau \rightarrow K\nu)}{\Gamma(\tau \rightarrow \pi\nu)} = 0.0653 \pm 0.0007. \quad (4.21)$$

This analysis, based upon a data sample which includes approximately 680000 $Z^0 \rightarrow q\bar{q}$ events (where this notation denotes the decay of a Z^0 to a quark-antiquark pair), found the $\tau^- \rightarrow K^- \nu_\tau$ branching ratio relative to the $\tau \rightarrow \pi(K)\nu$ branching ratio to be

$$\boxed{\frac{\Gamma(\tau \rightarrow K\nu)}{\Gamma(\tau \rightarrow \pi(K)\nu)} = 0.087 \pm 0.017_{-0.017}^{+0.016}} \quad (4.22)$$

where the first uncertainty is statistical and the second is systematic. This implies that the $\tau \rightarrow K\nu$ branching ratio relative to the $\tau \rightarrow \pi\nu$ branching ratio has a value of

$$\boxed{\frac{\Gamma(\tau \rightarrow K\nu)}{\Gamma(\tau \rightarrow \pi\nu)} = 0.095 \pm 0.020_{-0.020}^{+0.019}} \quad (4.23)$$

which is in agreement with the phenomenological prediction given in equation 4.21 (the two values differ by only approximately 1σ). The agreement between these two quantities implies that, to within the precision of this measurement, the phenomenology of Cabbibo-suppressed tau decays appears to be well described by the current model.

Over the next several years the OPAL experiment is expected to collect approximately $5 \times 10^6 Z^0 \rightarrow q\bar{q}$ events. This implies that the statistical error on this branching ratio measurement will be expected to go down from 19% of the branching fraction to 7%. The systematic errors of this measurement strongly depend on the statistics available and therefore these are also expected to decrease with increased statistics.

The $\tau \rightarrow \pi(K)\nu$ branching ratio has previously been measured by the OPAL experiment to be [14]:

$$Br(\tau \rightarrow \pi(K)\nu) = 0.122 \pm 0.003 \pm 0.004 \quad (4.24)$$

which, combined with equation 4.23, yields

$$Br(\tau \rightarrow K\nu) = 0.0106 \pm 0.0021^{+0.0020}_{-0.0021}$$

$$Br(\tau \rightarrow \pi\nu) = Br(\tau \rightarrow \pi(K)\nu) - Br(\tau \rightarrow K\nu) = 0.1113 \pm 0.0034 \pm 0.0040$$

The previous world averages for these quantities are [5]

$$Br(\tau \rightarrow K\nu) = 0.0067 \pm 0.0023$$

$$Br(\tau \rightarrow \pi\nu) = 0.116 \pm 0.004$$

Both the $\tau \rightarrow K\nu$ and $\tau \rightarrow \pi\nu$ branching ratio measurements are in agreement with the previous world averages and are also of comparable precision.

Chapter 5

Conclusions

This analysis found the $\tau^- \rightarrow K^- \nu_\tau$ branching ratio relative to the $\tau^- \rightarrow \pi^- \nu_\tau$ branching ratio to be

$$\frac{\Gamma(\tau \rightarrow K \nu)}{\Gamma(\tau \rightarrow \pi \nu)} = 0.095 \pm 0.020^{+0.019}_{-0.020}$$

The phenomenological prediction for this quantity derived from the branching ratios of $K^- \rightarrow \mu^- \bar{\nu}_\mu$ and $\pi^- \rightarrow \mu^- \bar{\nu}_\mu$ decays is

$$\frac{\Gamma(\tau \rightarrow K \nu)}{\Gamma(\tau \rightarrow \pi \nu)} = 0.0653 \pm 0.0007.$$

Both the prediction and the measurement derived by this analysis are in agreement (the two values differ by only approximately 1σ). This implies that, to within the precision of this measurement, Cabbibo-suppressed tau decays appear to be well described by the Standard Model and phenomenological predictions.

From the $\tau \rightarrow \pi(K) \nu$ branching ratio previously determined by the OPAL collaboration [14], $\tau \rightarrow K \nu$ and $\tau \rightarrow \pi \nu$ branching ratios were extracted. They were found to be

$$Br(\tau \rightarrow K \nu) = 0.0106 \pm 0.0021^{+0.0020}_{-0.0021}$$

and

$$Br(\tau \rightarrow \pi \nu) = 0.1113 \pm 0.0034 \pm 0.0040$$

The PDG92 world averages for these two quantities are [5]

$$Br(\tau \rightarrow K\nu) = 0.0067 \pm 0.0023 \quad \text{and} \quad Br(\tau \rightarrow \pi\nu) = 0.116 \pm 0.004$$

Both the $\tau \rightarrow K\nu$ and $\tau \rightarrow \pi\nu$ branching ratio measurements are in agreement with the previous world averages and are also of comparable precision.

Bibliography

- [1] G. Kane, *Modern Elementary Particle Physics*, Addison-Wesley, 1987.
- [2] F. Halzen and A. Martin, *Quarks and Leptons*, Wiley, 1984.
- [3] M. L. Perl et al, *Properties of Anomalous $e\mu$ Events Produced in e^+e^- Annihilation*, Physics Letters B63 (1976) 466.
- [4] G. J. Feldman et al, *Inclusive Anomalous Muon Production in e^+e^- Annihilation*, Physics Letters B63 (1976) 466.
- [5] L. S. Brown et al (Editors) *Review of Particle Properties*, Physical Review D 45 (1992).
- [6] G. B. Mills et al, *Measurement of the Cabibbo-Suppressed Decays $\tau^- \rightarrow K^- \nu_\tau$ and $\tau^- \rightarrow K^- \nu_\tau + n\pi^0$* , Physical Review Letters 52 (1984) 1944.
- [7] G. A. Blocker et al, *Measurement of the Branching Fraction for the Cabibbo Suppressed Decay $\tau^- \rightarrow K^- \nu_\tau$* , Physical Review Letters 48 (1982) 1586.
- [8] B. Barish et al, *The Physics of the Tau Lepton*, Physical Review Letters 157 (1988) 1.
- [9] K. Ahmet et al, the OPAL Collaboration, *The OPAL Detector at LEP*, Nuclear Instrumentation and Methods A305(1991) 275.
- [10] O. Biebel et al., *Performance of the OPAL jet chamber*, Nuclear Instrumentation and Methods A323(1992) 169.
- [11] M. Hauschild et al., *Particle Identification with the OPAL Jet Chamber*, Nuclear Instrumentation and Methods A314(1992) 74.
- [12] R. Fernow, *Introduction to Experimental Particle Physics*, Cambridge University Press, 1986.
- [13] J. Allison et al, the OPAL collaboration, *The Detector Simulation Program for the OPAL Experiment at LEP*, Nuclear Instrumentation and Methods A317(1992) 47.
- [14] G. Alexander et al, the OPAL collaboration, *Measurement of Branching Ratios and τ Polarization from $\tau^- \rightarrow e^- \bar{\nu}_e \nu_\tau$, $\tau^- \rightarrow \mu^- \bar{\nu}_\mu \nu_\tau$, and $\tau^- \rightarrow \pi^- (K^-) \nu_\tau$ Decays at LEP*, Physics Letters B266 (1991) 201.

Appendix A

Data Samples

The following is a discussion of the data samples used in this thesis. For more information on the systematics studies used to determine the background fractions in each of these samples, see reference [14].

All of the events in the data samples used in this analysis satisfy the following quality selection criteria:

- To ensure only well reconstructed charged tracks are used in this analysis, we require that:
 - * Each track must have at least 20 hits in the OPAL jet chamber with the first hit at a radius of no greater than 75 cm.
 - * The transverse momentum of each track must be at least 0.1 GeV/c.
 - * The distance of closest approach to the interaction point, $|d_0|$ and the z distance of closest approach to the interaction point, $|z_0|$, must both be at most 2 cm.
- To remove noisy calorimeter clusters we require:
 - * In the barrel region of the ECAL ($\cos(\theta) \leq 0.7$) there must be at least one hit block and the total raw cluster energy in the ECAL must be at least 0.1 GeV/c.

- * In the endcap region there must be at least two hit blocks in the ECAL and a total raw cluster energy at least 0.2 GeV/c. In addition we require the fraction of the energy in the ECAL block containing the most energy to the total raw cluster energy to be less than 0.99.

A.1 Selection of $e^+e^- \rightarrow \tau^+\tau^-$ Candidates

To select $e^+e^- \rightarrow \tau^+\tau^-$ candidates we require the following selection criteria:

- To remove hadronic backgrounds resulting from $Z^0 \rightarrow q\bar{q}$ events (where q denotes a quark), we require there to be between 1 and 6 charged tracks per event and less than 10 ECAL clusters associated with each event.
- Since τ decays are characterized by two back to back *jets* of particles, it is often convenient to assign charged tracks and ECAL clusters in τ decays to cones. For $e^+e^- \rightarrow \tau^+\tau^-$ candidates we require that the cones be of half angle 35° , that the total track and ECAL cluster assigned to each cone be at least $0.01 * E_{beam}$, and that there be only two charged cones in the event.
- In order to reject cosmic rays, we require the following:
 - * At least one good charged track in the event must have $|d_0| < 0.5$ cm and $|z_0| < 20$ cm.
 - * The difference between the measured TOF and the expected TOF flight for a track (assuming the track originated at the origin) must be no less than 10 ns. An event is also *rejected* if all TOF counter pairs separated by at least 165° in ϕ have TOF readings which are different by at least 10 ns.

- To remove two photon events, we exploit the low visible energies and low net transverse momentum typical of $e^+e^- \rightarrow (e^+e^-)X$ events.

An event is *rejected* if the sum of the visible energies of the jets, E_{vis} , is less than 3% of E_{CM} . E_{vis} is defined as

$$E_{vis} \equiv \sum_{cone} \max(E_{cls}, E_{trk})$$

where E_{trk} and E_{cls} are the track and cluster energy associated with each track.

Also, if E_{vis} is less than 20% of E_{CM} , the event will be *rejected* if the missing transverse momenta, calculated separately for both the charged tracks and ECAL clusters, are both less than 2 GeV/c.

- To remove background from Bhabha events, the large energy deposition in the electromagnetic calorimeter typical of such events is exploited. An event is *rejected* if

$$\sum_i E_i^{CLUST} > 0.8E_{CM}$$

and

$$\sum_i E_i^{CLUST} + 0.3 \sum_j E_j^{TRACK} > E_{CM}$$

where the summation is over all good clusters and tracks in the event.

- Rejection of $e^+e^- \rightarrow \mu^+\mu^-$ and $e^+e^- \rightarrow \mu^+\mu^-\gamma$ backgrounds depends mainly upon the muon identification provided by the ECAL, HCAL, and MUON detectors and on the high track momentum typical of such events. An event is *rejected* if it contains two muon candidates and if the scalar sum of the charged track momenta plus the energy of the most energetic ECAL cluster in each cone is greater than $0.6E_{CM}$. A muon candidate must satisfy one of the following three requirements:

MUID :

Muon identification by the outer four MUON chamber layers. In order to meet this requirement the track must have

at least two layers in the barrel or endcap MUON detector with signals associated with the track.

HCID :

Muon identification by the hadron calorimeter. In order to meet this requirement the track must have at least 4 layers in HCAL with signals associated with the track, with at least one of the layers being in the last three layers of the HCAL. Also the ratio of the total number of HCAL layers assigned to the jet to the number of HCAL layers assigned to the track must be less than three.

ECID :

Muon identification by the electromagnetic calorimeter. In order to meet this requirement the ECAL cluster energy associated with the track must be less than 2 GeV.

These requirements selected a final sample of 11381 τ pair candidates with an estimated background fraction of 0.019 ± 0.007 and an efficiency of $54.1 \pm 0.2\%$ (which corresponds to an efficiency of 93% within the geometrical acceptance)..

A.1.1 Selection of $\tau^- \rightarrow \mu^- \bar{\nu}_\mu \nu_\tau$ Candidates

The $\tau^- \rightarrow \mu^- \bar{\nu}_\mu \nu_\tau$ candidates must satisfy the following requirements:

- There must be exactly one charged track per candidate jet.
- Most $\tau^- \rightarrow \mu^- \bar{\nu}_\mu \nu_\tau$ decays are characterized by a small energy deposition in the ECAL and associated signals in the HCAL and MUON subdetectors consistent with the passage of minimum ionizing particle. In order to

accept muons that enter inactive regions of the HCAL or MUON subdetectors, or that are accompanied by radiation, however, it is only required that a $\tau^- \rightarrow \mu^- \bar{\nu}_\mu \nu_\tau$ candidate satisfy at least two out of **MUID**, **HCID**, and **ECID** defined above.

- Any associated signals in the HCAL must be consistent with the passage of a minimum ionizing particle, even when the **HCID** condition is not satisfied. Thus a $\tau^- \rightarrow \mu^- \bar{\nu}_\mu \nu_\tau$ candidate is *rejected* if the number of layers in HCAL associated with the track is at least three and if the ratio to the total number of HCAL layers assigned to the jet to those assigned to the track is at least three.
- Some residual background from hadronic decays accompanied by π^0 production is suppressed by requiring

$$M_{trk-ecal} < 0.3 GeV$$

where $M_{trk-ecal}$ is the invariant mass of the charged track (assuming a π^\pm hypothesis) and all ECAL clusters in the jet (assuming a photon hypothesis). In the calculation 0.5 GeV is subtracted from the energy and momentum of the ECAL cluster nearest the charged track to account for the energy deposition expected from a minimum ionizing particle.

- In order to suppress residual $e^+e^- \rightarrow \mu^+\mu^-$ contamination, a $\tau^- \rightarrow \mu^- \bar{\nu}_\mu \nu_\tau$ candidate is rejected if the *opposite* jet consists of exactly one charged track, consistent with being a muon, that satisfies

$$p_{trk} + E_{cls} - 0.5 GeV \geq 0.8 E_{beam}$$

where 0.5 GeV is the average ECAL energy deposition of a minimum ionizing particle. A track is considered consistent with being a muon if it satisfies any *one* of the following criteria:

1. **MUID** identification (defined above).
2. **HCID** identification (defined above).
3. Passage through a geometric region where neither the hadron calorimeter nor the MUON chambers are fully active.

Background	Contamination(%)
$\tau \rightarrow \pi(K)\nu$	2.4 ± 0.5
$\tau \rightarrow other$	0.3 ± 0.2
$e^+e^- \rightarrow \mu^+\mu^-$	0.7 ± 0.1
$e^+e^- \rightarrow e^+e^-\mu^+\mu^-$	0.7 ± 0.1
TOTAL	3.71 ± 0.60

Table A.7: Estimated background contaminations found in the selected $\tau^- \rightarrow \mu^- \bar{\nu}_\mu \nu_\tau$ candidate events in the 1990 and 1991 data.

- To ensure reliable muon identification with low background, the muon candidates must satisfy:

$$\frac{(p_{trk} + E_{cls} - 0.5GeV)}{E_{beam}} > 0.05.$$

There were 3798 $\tau^- \rightarrow \mu^- \bar{\nu}_\mu \nu_\tau$ candidates in the combined 1990 and 1991 data samples and the backgrounds estimated from Monte Carlo and dedicated data studies are shown in table A.7.

A.1.2 Selection of $\tau^- \rightarrow \pi^- (K^-) \nu_\tau$ Candidates

The $\tau^- \rightarrow \pi^- (K^-) \nu_\tau$ candidates must satisfy the following criteria:

- There must be exactly one good charged track assigned to the jet cone.
- To reject $\tau^- \rightarrow e^- \bar{\nu}_e \nu_\tau$ and other backgrounds with large associated ECAL energy, the ratio of energy, E_{cls} , of the cluster associated with the pion candidate to the candidate's reconstructed track momentum, p_{trk} , must satisfy:

$$E_{cls}/p_{trk} < 0.8.$$

- To reject hadronic decays accompanied by $\pi^0 \rightarrow \gamma\gamma$, it is required that the total cluster energy in the jet, excluding the cluster associated with the pion candidate track, satisfy:

$$E_{excess} < 0.02 E_{beam}$$

- Further rejection of hadronic backgrounds accompanied by π^0 's is obtained by requiring the difference in azimuth, $\delta\phi_{Max}$, between the track and pre-sampler signal *farthest* away in azimuth (but still assigned to the jet) to be less than 0.5° .
- Removing the background from $\tau^- \rightarrow \mu^- \bar{\nu}_\mu \nu_\tau$ depends critically upon the HCAL and MUON chambers, both of which have some geometric gaps in acceptance. Only $\tau^- \rightarrow \pi^- (K^-) \nu_\tau$ candidates in the region of full response of the MUON chambers are accepted. If the candidate enters a region where the HCAL is also fully active then it is *rejected* if either

$$N_{layers}^{HC/MU} \geq 3$$

or the following two conditions are met

$$N_{layers}^{HC/MU} = 2$$

and

$$N_{hits/layer}^{HC} < 3$$

where $N_{layers}^{HC/MU}$ is the number of layers containing signals out of a possible seven in the HCAL (three layers) and MUON (four layers) subdetectors. If the candidate enters a region where the HCAL is not fully active then it is rejected if

$$N_{layers}^{MU} \geq 2$$

where N_{layers}^{MU} is the number of MUON chamber layers associated with the signal.

- To ensure good understanding of $\tau^- \rightarrow \pi^- (K^-) \nu_\tau$ selection efficiency and backgrounds, the candidate's track momentum must satisfy

$$\frac{p_{trk}}{E_{beam}} > 0.05.$$

There were 1242 $\tau^- \rightarrow \pi^- (K^-) \nu_\tau$ candidates in the combined 1990 and 1991 data sample and the backgrounds estimated from Monte Carlo and dedicated data studies are shown in table A.8.

Background	Contamination(%)
$\tau^- \rightarrow e^- \bar{\nu}_e \nu_\tau$	1.5 ± 0.3
$\tau^- \rightarrow \mu^- \bar{\nu}_\mu \nu_\tau$	0.3 ± 0.1
$\tau^- \rightarrow \rho \nu_\tau$	4.1 ± 0.4
$\tau \rightarrow other$	1.7 ± 0.2
TOTAL	7.6 ± 0.7

Table A.8: Estimated background contaminations found in the selected $\tau^- \rightarrow \pi^- (K^-) \nu_\tau$ candidate events in the 1990 and 1991 data.

VITA

Surname: **TOWERS**

Given Names: **Sherry Meleah Jean**

Place of Birth: **Kitimat, B. C.**

Date of Birth: **April 1st, 1967**

Educational Institutions Attended

University of Victoria	1991 to 1993
Simon Fraser University	1985 to 1991

Degrees Awarded

B. Sc. (Honours)	Simon Fraser University	1991
------------------	-------------------------	------

Honours and Awards

University of Victoria Graduate Teaching Fellowship	1992/1993
University of Victoria Graduate Teaching Fellowship	1991/1992
NSERC Undergraduate Research Award	1991
NSERC Undergraduate Research Award	1990
NSERC Undergraduate Research Award	1989

Publications

B. Aubert et al, *Performance of a Liquid Argon Calorimeter with Fast Read-Out*, Nuclear Instruments and Methods, A321(1992), 467-478.

PARTIAL COPYRIGHT LICENSE

I hereby grant the right to lend my thesis to users of the University of Victoria Library, and to make single copies only for such users or in response to a request from the Library of any other university, or similar institution, on its behalf or for one of its users. I further agree that permission for extensive copying of this thesis for scholarly purposes may be granted by me or a member of the University designated by me. It is understood that copying or publication of this thesis for financial gain shall not be allowed without my written permission.

Title of Thesis: A Measurement of the $\tau^- \rightarrow K^- \nu_\tau$ Branching Ratio Using the OPAL Detector at LEP

Author



SHERRY MELEAH JEAN TOWERS

(Name in Block Letters)

July 2nd 1993

(Date)